


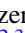







Taking a Long Look: A Two-decade Reverberation Mapping Study of High-luminosity Quasars

Shai Kaspi¹ , W. N. Brandt^{2,3,4} , Dan Maoz¹ , Hagai Netzer¹ , Donald P. Schneider^{2,3} , Ohad Shemmer⁵ , and C. J. Grier^{2,3,6} 

¹ School of Physics and Astronomy and Wise Observatory, Raymond and Beverly Sackler Faculty of Exact Sciences, Tel-Aviv University, Tel-Aviv 69978, Israel
shaik@tauex.tau.ac.il

² Department of Astronomy and Astrophysics, 525 Davey Laboratory, Pennsylvania State University, University Park, PA 16802, USA

³ Institute for Gravitation and the Cosmos, The Pennsylvania State University, University Park, PA 16802, USA

⁴ Department of Physics, The Pennsylvania State University, University Park, PA 16802, USA

⁵ Department of Physics, University of North Texas, Denton, TX 76203, USA

⁶ Steward Observatory, The University of Arizona, 933 North Cherry Avenue, Tucson, AZ 85721, USA

Received 2021 January 21; revised 2021 May 8; accepted 2021 May 10; published 2021 July 16

Abstract

Reverberation mapping (RM) of active galactic nuclei (AGNs) has been used over the past three decades to determine AGN broad-line region (BLR) sizes and central black hole masses, and their relations with the AGN luminosity. Until recently, the sample of objects with RM data was limited to low-luminosity AGNs ($L_{\text{opt}} \lesssim 10^{46} \text{ erg s}^{-1}$) and low redshifts ($z \lesssim 0.5$). Here we present results from an RM project of some of the most luminous and highest-redshift quasars that have been mapped to date. The study is based on almost 20 years of photometric monitoring of 11 quasars, 6 of which were monitored spectrophotometrically for 13 yr. This is the longest RM project carried out so far on this type of AGNs. We successfully measure a time lag between the C IV λ 1549 broad emission line and the quasar continuum in three objects, and measure a C III] λ 1909 lag in one quasar. Together with recently published data on C IV RM, the BLR size is found to scale as the square root of the UV luminosity over eight orders of magnitude in AGN luminosity. There is a significant scatter in the relation, part of which may be intrinsic to the AGNs. Although the C IV line is probably less well suited than Balmer lines for determination of the mass of the black hole, virial masses are tentatively computed, and in spite of a large scatter, we find that the mass of the black hole scales as the square root of the UV luminosity.

Unified Astronomy Thesaurus concepts: Active galactic nuclei (16); Active galaxies (17); Galaxy nuclei (609); High-luminosity active galactic nuclei (2034); Low-luminosity active galactic nuclei (2033); Quasars (1319)

Supporting material: machine-readable tables

1. Introduction

Over the past three decades the reverberation-mapping (RM) technique has been used to determine the size of the broad-line region (BLR) in active galactic nuclei (AGNs) and to infer their black hole (BH) masses in about 200 objects (for reviews, see Peterson 1993, Peterson 2006; Netzer & Peterson 1997, and references therein). RM uses the response of the emission lines from the BLR to continuum variations and measures the time lag of the response, which is interpreted as an estimate of the light-travel time, and hence the physical separation, between the BH and the bulk of the BLR gas. A recent compilation of RM objects can be found in Bentz & Katz (2015)⁷, Du et al. (2015, 2016, 2018), Shen et al. (2016), and Grier et al. (2017, 2019).

Almost all reverberation-mapping studies have focused on low-redshift AGNs with optical luminosities ($\lambda L_{\lambda}(5100\text{\AA})$) lower than $10^{46.5} \text{ erg s}^{-1}$. RM of high-luminosity AGNs is quite challenging; their BLR sizes are expected to be large and their continuum variations are slow. Combining these features with the cosmological time dilation at high redshift, RM campaigns must span a period of a decade or more, necessitating very long-term commitment of observing facilities. In addition, large telescope collecting areas are required because these quasars are faint.

Several early RM efforts for high-luminosity quasars were unsuccessful at detecting reverberation time lags, e.g., Welsh et al. (2000), Trevese et al. (2006, 2007), and A. Marconi (2005, private communication), due to the insufficient duration of these projects. Trevese et al. (2014) reported 11 yr of monitoring of the $z = 2.048$ quasar PG 1247+267; however, their sampling was poor (one to three points a year), and the model-independent methods used to derive the time lag are not sufficiently accurate: using the model-dependent⁸ method of stochastic process estimation for AGN reverberation (SPEAR) developed by Zu et al. (2011), they claimed a significant time-lag measurement that we consider questionable, however. Saturni et al. (2016) reported an RM study of APM 08279+5255 over 12 yr, also with a rather limited sampling rate. They use the model-dependent JAVELIN method (Zu et al. 2013), a development of SPEAR, to estimate the time lag. Inspection of their Figure 4 shows that the use of JAVELIN introduces several model points inside long gaps in the data, i.e., there are no real overlapping measurements in the data used to determine the lag. This greatly lowers the significance of this result, and we do not consider it further here.

Shen et al. (2016) have reported preliminary results of 15 BLR lag measurements from the Sloan Digital Sky Survey Reverberation Mapping (SDSS-RM) project. The project targets almost 850

⁷ See the website <http://www.astro.gsu.edu/AGNmass/>.

⁸ In that it adopts a reasonable damped random walk-based interpolation approach, see Yu et al. (2020) and Li et al. (2019).

AGNs with redshifts up to $z=4.5$ and expects to deliver BLR lag measurements for a few hundred. The reported preliminary lag measurements are for intermediate-luminosity quasars at $0.3 \lesssim z < 0.8$ and include nine $H\beta$ lags and six $Mg\ II$ lags. Further BLR lag measurements from that project have been reported by Grier et al. (2017), who measured $H\beta$ and $H\alpha$ BLR lag measurements for a total of 44 and 18 quasars, respectively, at the redshift range of $0.1 < z < 1.1$. They find that in most objects, the time delay of the $H\alpha$ emission is consistent with or slightly longer than that of $H\beta$. Their BH mass measurements are mostly consistent with expectations from single-epoch BH mass measurements and the local $M_{BH}-\sigma_*$ relation.

Lira et al. (2018) describe an RM project that targeted 17 high-luminosity quasars for more than 10 yr. These authors are able to measure statistically significant ($> 1\sigma$) time lags for the emission lines of $Ly\alpha$ (8 objects), $C\ IV$ (8 objects), $Si\ IV$ (3 objects), and $C\ III]$ (1 object). Altogether, significant time lags were measured for 10 distinct objects. Lira et al. (2018) give an updated $C\ IV$ radius–luminosity relation, and presented for the first time a radius–luminosity relation for the other three lines. They report that the regions responsible for the emission of $Ly\alpha$, $Si\ IV$, $C\ IV$, and $C\ III]$ are commonly interior to that producing $H\beta$, but there is no clear stratification among them. Approximately 18% (3/17) of their sources show an unexpected behavior in some emission lines in which the line light curves do not appear to follow the observed UV continuum variations. This is similar to the recent behavior detected in the AGN NGC 5548, in which during a monitoring of 180 days the BLR had a period of ~ 40 days in which it did not follow the UV continuum variations (Goat et al. 2019).

Hoormann et al. (2019) report $C\ IV$ RM time lags for two objects from the Dark Energy Survey Supernova Program (DES-SN) and the Australian Dark Energy Survey (OzDES) at redshifts of 1.9 and 2.6. In this study, the photometric monitoring covers 5 yr, while the spectroscopic monitoring was 3–4 yr. Out of the 393 objects with $C\ IV$ in their sample, they identified a subset of objects that were expected to have lags of about 1 yr. They further cut the sample to 23 objects that were variable and had high-cadence data, but only 2 of them had significant time-lag measurements.

In a recent paper, Grier et al. (2019) report on $C\ IV$ RM time lags from the SDSS-RM project. They report time lags for 52 AGNs, with an estimated false-positive detection rate of 10%. Sixteen of these AGNs are defined as their “gold sample” with the highest-confidence lag measurements. These 16 AGNs lay in the redshift range of $1.4 < z < 2.8$ and luminosity range of $10^{44.5} < \lambda_{L\lambda}(1350\text{\AA}) < 10^{45.6}$ erg s $^{-1}$. Adding these 16 objects to the objects with $C\ IV$ time-lag measurements of previous studies, they find that the radius–luminosity relation has a slope of 0.52 ± 0.04 . Shen et al. (2019) show that adding photometric data to the spectroscopic monitoring of this project can improve the detection of time lags. They report on three more objects with detected $C\ IV$ time lags.

In Kaspi et al. (2007; hereafter Paper I) we presented the first results from our RM campaign of several high-luminosity AGNs. In this paper we report the final results from this campaign after 18 yr of photometric and 13 yr of spectroscopic monitoring. This is the longest single RM campaign carried out to date (only one object surpasses this, the multiple campaigns on NGC 5548 over the past two decades). Section 2 describes the observations and the data-reduction process. Section 3 presents the results. Section 4 analyzes the new results,

Table 1
Luminosities

Object	$\lambda_{L\lambda}(1350\text{\AA})^a$	$\lambda_{L\lambda}(5100\text{\AA})^a$	R^b
S5 0014+81	7.66 ± 1.00	3.94	493.3
S5 0153+74	1.20 ± 0.20	0.62	12377.8
S4 0636+68 ^c	3.66 ± 0.26	1.88	133.2
S5 0836+71 ^c	1.03 ± 0.16	0.53	10064.5
TB 0933+733	1.57 ± 0.18	0.81	5.2
SBS 1116+603 ^c	1.79 ± 0.20	0.92	632.7
SBS 1233+594 ^c	1.98 ± 0.18	1.02	1.3
SBS 1425+606 ^c	4.54 ± 0.37	2.34	4.6
HS 1700+6416 ^c	5.00 ± 0.34	2.57	3.6
HS 1946+7658	10.9 ± 1.22	5.63	1.7
S5 2017+744	0.72 ± 0.09	0.37	2765.8

Notes. $\lambda_{L\lambda}(1350\text{\AA})$ for the six objects in our spectroscopic sample were measured from the spectra shown in Figure 1, for S5 0014+81, S5 0153+74, and HS 1946+7658 from spectra published in the literature, and for TB 0933+733 and S5 2017+74 from extrapolation of their SED given in NED. Luminosities were corrected for Galactic extinction using A_V from NED based on Schlafly & Finkbeiner (2011). $\lambda_{L\lambda}(5100\text{\AA})$ was computed from $\lambda_{L\lambda}(1350\text{\AA})$ using a power law $f_\nu \propto \nu^{-0.5}$.

^a In units of 10^{47} erg s $^{-1}$.

^b Radio loudness is the radio (1.4 GHz)-to-optical (estimated at 4400 \AA) flux ratio, from Paper I.

^c Spectroscopically monitored.

combined with the results of other RM campaigns of high-luminosity AGNs that have yielded significant results.

Throughout this paper we use the standard cosmology with $H_0 = 70$ km s $^{-1}$ Mpc $^{-1}$, $\Omega_M = 0.3$, and $\Omega_\Lambda = 0.7$.

2. Sample, Observations, and Data Reduction

The sample, observations, and data processing are described in detail in Paper I. For completeness, we summarize them here and note differences where applicable.

The photometric sample consists of 11 high-luminosity quasars with observed magnitude of $V \lesssim 18$ and redshift in the range $2 \lesssim z \lesssim 3.4$. The luminosity range is $10^{46.9} \lesssim \lambda_{L\lambda}(1350\text{\AA}) \lesssim 10^{48.0}$ erg s $^{-1}$, which translates into $10^{46.6} \lesssim \lambda_{L\lambda}(5100\text{\AA}) \lesssim 10^{47.8}$ erg s $^{-1}$ (see Table 1 for details). Six of the objects in our sample are radio loud and five are radio quiet (see Paper I for details). All objects are at high decl. ($\delta \gtrsim +60^\circ$) to enable largely uninterrupted yearly coverage from the Northern Hemisphere.

Photometric observations were obtained at the Wise observatory 1 m telescope in the Johnson-Cousins B and R bands from 1995 to mid-2013. The only difference from the description of Paper I is that during 2006, the Tektronix CCD was replaced with a Princeton Instruments camera with a E2V 1300×1340 CCD that had similar field of view and quantum efficiency; exposure time and sampling rate were unchanged from the description in Paper I. Exposure times for all objects were 250 and 300 s in the R and B bands, respectively, except that for S5 2017+744, we used 300 and 400 s. Each object was observed photometrically about once a month for eight months each year. Photometric uncertainties are about 0.03 mag. The data have been reduced using IRAF⁹ procedures in the standard way.

⁹ IRAF (Image Reduction and Analysis Facility) is distributed by the National Optical Astronomy Observatories, which are operated by AURA, Inc., under cooperative agreement with the National Science Foundation.

Spectroscopic observations were performed for 6 of the 11 photometrically monitored AGNs at the Hobby-Eberly Telescope (HET; Ramsey et al. 1998). Spectra were obtained starting in 1999 with the Low Resolution Spectrograph (LRS; Hill et al. 1998), which began its primary observations in 1998, and spectroscopic observations continued until the instrument was decommissioned in mid-2013. Spectra were taken with a long slit that included the AGN and a field star that was used for flux calibration. Observations typically consisted of two consecutive exposures of the quasar/star pair with exposure times (for each exposure) of 900 s for S4 0636+68 and SBS 1116+603, 600 s for S5 0836+71 and SBS 1233+594, and 300 s for SBS 1233+594 and HS 1700+6416 (three of these objects are radio-loud AGNs and three are radio-quiet AGNs). We observed each of the six objects about three to four times each year with a separation of two to three months between observations. The total program time amounted to roughly 12 hr of HET time each year (including overheads). The spectroscopic data were processed using standard IRAF routines as described in Paper I.

Figure 1 shows the mean and rms¹⁰ spectra of the six spectroscopically monitored quasars. We used the mean and rms spectra to identify line-free spectral bands that are suitable for setting the continuum underlying the emission lines, and the wavelength limits for integrating the line fluxes. The spectral ranges for the lines and the continuum bands on both sides of each line are given in Table 2. The detailed measurement process is as described in Kaspi et al. (2000) and in Paper I.

3. Results

3.1. Continuum and Line Light Curves

Information about the light curves for the six spectroscopically monitored objects is given in Table 3. The light curves are presented in Figure 2–7 with the data listed in Tables 4 and 5. The photometric *R*-band light curves were merged with the spectroscopic continuum light curves as described in Paper I in order to increase the sampling of the continuum light curve. The different bands used for the flux measurements are listed in Table 2 for each object (wavelengths are given in the observed frame). The number of observations as well as statistical information about the light curves are provided in the upper part of Table 3. Columns are (1) the object name, (2) the particular light curve, (3) the number of points in that light curve, (4), (5), and (6) the mean (\bar{f}), rms (σ), and the mean uncertainty (δ) of all data points in the light curves, respectively, in the appropriate units for each light curve, (7) the χ^2_ν obtained by fitting a constant to the light curve, and (8) $P(\chi^2_\nu)$, the probability of obtaining this χ^2 if there were intrinsically no variability. This test is used to determine whether the light curve is consistent with a constant flux to a significance level of 95%. For light curves that show significant variability, Column (9) lists the intrinsic normalized variability measure, $\sigma_N = 100\sqrt{\sigma^2 - \delta^2}/\bar{f}$ (used by Kaspi et al. 2000), and Column (10) is the fractional variability amplitude, F_{var} , and its uncertainty (e.g., Rodríguez-Pascual et al. 1997; Edelson et al. 2002), which are defined as $F_{\text{var}} = \sqrt{\sigma^2 - \langle \sigma_{\text{err}}^2 \rangle} / \bar{f}$ and $\sigma_{F_{\text{var}}} = \sqrt{1/(2N)} \sigma^2 / (\bar{f}^2 F_{\text{var}})$, respectively, where $\langle \sigma_{\text{err}}^2 \rangle$ is the mean error squared.

Further discussion of the photometric light curves as well as the *B*-band light curves of these objects are given in the Appendix.

All light curves as well as individual and mean spectra are also available at doi:10.5281/zenodo.4718461 and at the website: <http://wise-obs.tau.ac.il/~shai/highz/>.

3.2. Time-series Analysis

In order to measure a time lag that can serve as an estimate for the BLR size, one usually cross correlates the line and continuum light curves. Two commonly used methods were applied. The first is the interpolated cross-correlation function (ICCF; Gaskell & Sparke 1986 and Gaskell & Peterson 1987 as implemented by White & Peterson 1994). In this approach, one light curve is cross correlated with a linear interpolation of the second light curve, then the second light curve is cross correlated with a linear interpolation of the first light curve, and then the final cross correlation is the average of these two cross-correlation functions. The time lag is then determined as the centroid of all points in the ICCF with a correlation value above 80% of the peak correlation value.

The second method is the *z*-transformed discrete correlation function (ZDCF; Alexander et al. 1997), which is an improvement of the discrete correlation function (DCF) method suggested by Edelson & Krolik (1988). The ZDCF applies Fisher’s *z* transformation to the correlation coefficients and uses equal population bins instead of the equal time bins that are used in the DCF. We also applied the JAVELIN method to our data. JAVELIN (Zu et al. 2013) uses the assumption that all emission-line light curves are scaled, smoothed, and displaced versions of the continuum. It fits the light curves directly using a damped random-walk model and aligns them to recover the time lag and its statistical confidence limits. We find that with our detailed light curves, JAVELIN produces similar results to the ICCF and ZDCF methods. In the following, we refer only to the first two methods.

Figures 2–7 present the ICCF and ZDCF of the two lines (out of the three lines Ly α , C III], and C IV) that were monitored in each object. We consider a time lag as significant¹¹ if the CCF possesses a maximum with a peak correlation larger than 0.5 (e.g., Kaspi et al. 2000; Lira et al. 2018) in both the ICCF and ZDCF, and that it is a result of a significant overlap of the continuum and line light curves. We then calculated the uncertainties on the time lags of the ICCF method using the model-independent Monte Carlo method flux randomization/random subset selection (FR/RSS) of Peterson et al. (1998). This method yields a cross-correlation centroid distribution (CCCD) of the time lags found in the Monte Carlo simulations of the light curves, and this distribution is used to estimate the uncertainties. The CCCDs for our time lags are shown in Figure 8. The range of uncertainty is taken as the range that includes the central 68% of the CCCD realizations, i.e., 16% at the two edges of the distribution are omitted and the central range determines the uncertainty range. This is demonstrated by the vertical dashed lines in Figure 8. Once the uncertainty range is determined, the centroid of the ICCF, of the full two light curves, is taken as the time lag, and its plus and minus uncertainties are calculated to encapsulate this uncertainty range.

¹⁰ As defined in Equation (1) of Paper I.

¹¹ Further discussion of the significance is given at the end of Section 3.3.7.

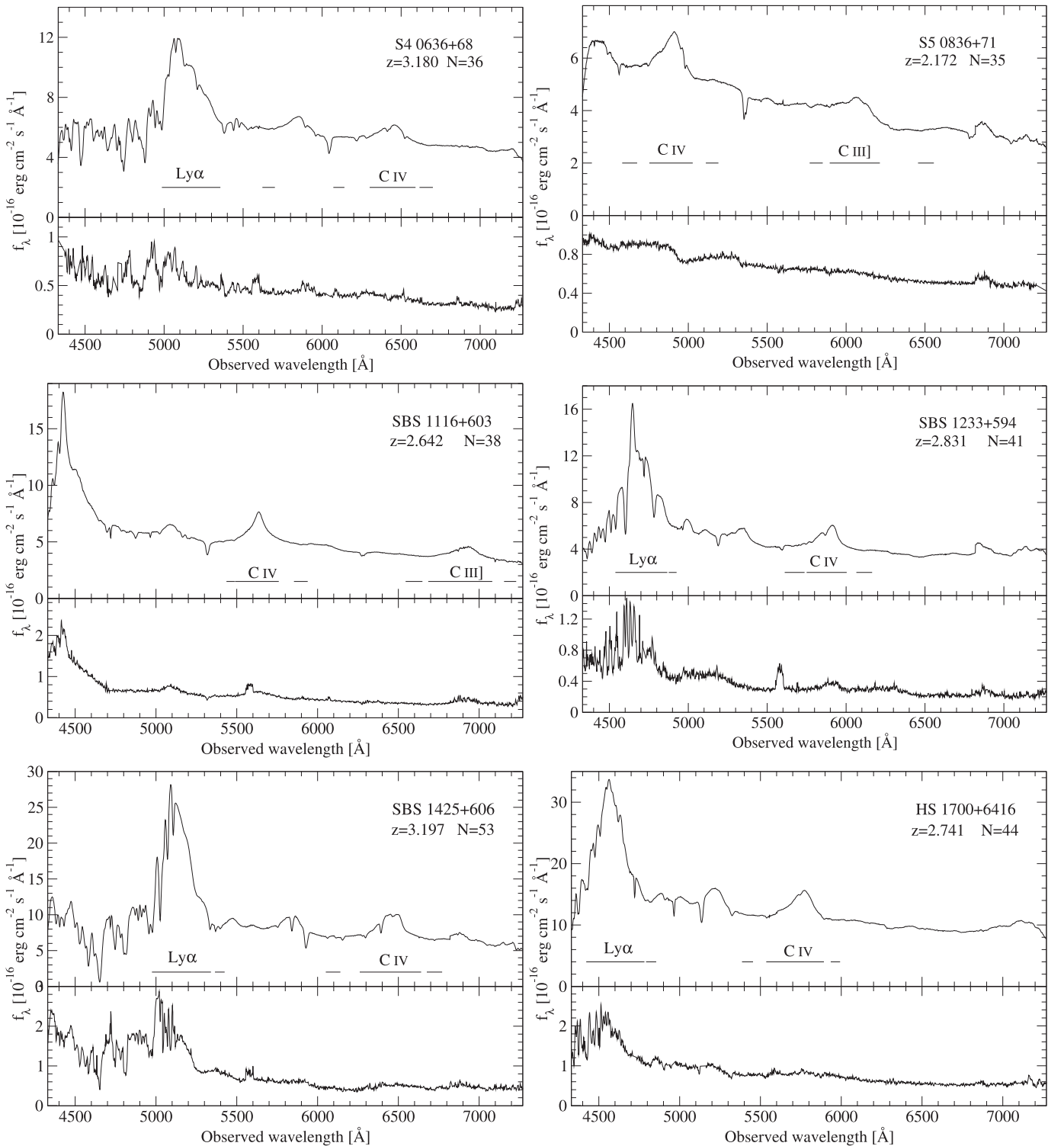


Figure 1. Mean (top panels) and rms (bottom panels) spectra for the six objects in our sample. Under each object name the redshift (z) and the number of spectra (N) used in the mean and rms are given. Vertical lines in the top panels show the integration ranges for continuum bands and emission lines as listed in Table 2. Emission lines are labeled, and continuum bands have no labels.

He II $\lambda 1640$ is usually a weak line relative to C IV $\lambda 1550$ in high-luminosity AGNs. This is evident from the mean spectra shown in Figure 1, where the line is absent or barely detected. This is also shown in Dietrich et al. (2002). Although they find the Baldwin relation (Baldwin 1977) is about the same for both lines, the flux of the He II $\lambda 1640$ line in their composite quasar spectra is much weaker than the C IV $\lambda 1550$ flux. The

He II $\lambda 1640$ line falls outside of the measured ranges listed in Table 2, so this line does not affect our measured C IV time lag.

3.3. Notes on Individual Objects

The reported significant C IV time lags are listed in Table 6. Here we list notes on the time lags found in individual objects.

Table 2
Integration Limits for Continuum Bands and Emission Lines

Object (1)	Ly α (2)	Continuum ^a (3)	Continuum (4)	C IV (5)	Continuum (6)	Continuum (7)	C III] (8)	Continuum (9)
S4 0636+68	4986-5356	5622-5701	6071-6141	6301-6591	6616-6701
S5 0836+71	4581-4676	4753-5028	5111-5191	5769-5852	5896-6214	6456-6556
SBS 1116+603	5436-5487	5489-5760	5854-5939	6545-6649	6685-7061	7154-7220
SBS 1233+594	4538-4867	4876-4926	5611-5737	5750-6004	6065-6165
SBS 1425+606	4975-5340	5365-5415	6051-6141	6261-6641	6676-6771
HS 1700+6416	4422-4782	4792-4855	5386-5454	5536-5893	5935-5993

Note. Wavelengths are in units of \AA in the observer's frame. The boldface ranges are the continuum bands used for the cross-correlation analysis.

^a Due to the noisy absorbed spectrum on the blue side of Ly α , only the continuum on the red side was used to define the continuum underlying this line.

Table 3
Variability Measures

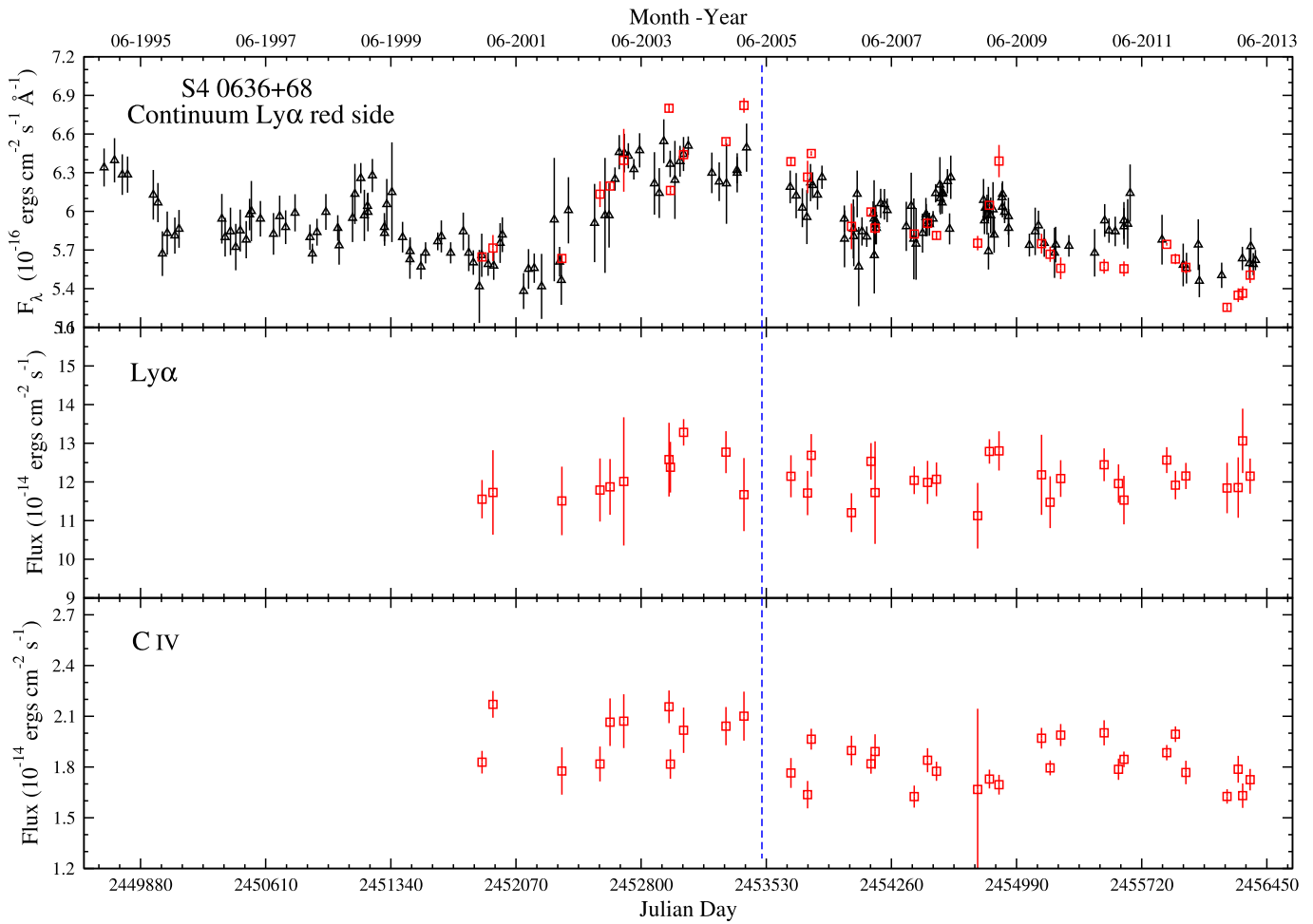
Object (1)	Light Curve (2)	N^a (3)	Mean ^b (4)	rms ^b (5)	Mean Uncertainty ^b (6)	χ^2_ν (7)	$P(\chi^2 \nu)^c$ (8)	σ_N (9)	F_{var} (10)
Spectroscopically Monitored Objects									
S4 0636+68	continuum	209	5.94	0.28	0.14	26.53	0	4.15	0.040 ± 0.003
	Ly α	36	12.09	0.51	0.67	1.04	0.40
	C IV	36	1.86	0.15	0.09	4.25	0	4.70	0.054 ± 0.015
	<i>B</i>	169	17.203	0.061	0.033	4.69	0	4.81	0.045 ± 0.004
S5 0836+71	continuum	181	3.18	0.45	0.08	162.13	0	13.95	0.138 ± 0.008
	C IV	35	2.26	0.41	0.10	14.95	0	17.41	0.173 ± 0.022
	C III]	35	1.06	0.28	0.08	14.19	0	25.08	0.250 ± 0.033
	<i>B</i>	144	17.199	0.178	0.031	54.35	0	16.84	0.167 ± 0.010
SBS 1116+603	continuum	201	3.14	0.34	0.09	27.63	0	10.59	0.105 ± 0.006
	C IV	38	3.01	0.36	0.09	19.81	0	11.53	0.115 ± 0.014
	C III]	38	1.89	0.29	0.12	5.52	0	13.71	0.135 ± 0.019
	<i>B</i>	154	17.421	0.132	0.034	20.32	0	11.60	0.115 ± 0.007
SBS 1233+594	continuum	198	4.00	0.27	0.09	33.10	0	6.30	0.062 ± 0.004
	Ly α	41	12.62	0.84	1.26	0.56	1.00
	C IV	41	2.40	0.19	0.09	5.78	0	6.87	0.067 ± 0.010
	<i>B</i>	158	17.758	0.094	0.037	7.64	0	7.89	0.077 ± 0.005
SBS 1425+606	continuum	228	6.84	0.45	0.14	28.22	0	6.24	0.061 ± 0.003
	Ly α	53	32.99	1.48	2.01	0.41	1.00
	C IV	53	5.95	0.35	0.23	2.24	7.7×10^{-7}	4.53	0.044 ± 0.008
	<i>B</i>	170	17.278	0.102	0.030	16.08	0	8.97	0.089 ± 0.005
HS 1700+6416	continuum	247	10.61	0.69	0.23	33.80	0	6.14	0.060 ± 0.003
	Ly α	44	30.05	1.31	2.04	0.91	0.65
	C IV	45	6.86	0.41	0.24	3.46	0	4.86	0.047 ± 0.008
	<i>B</i>	197	16.068	0.072	0.026	10.83	0	6.23	0.061 ± 0.004
Photometrically Monitored Objects									
S5 0014+81	<i>R</i>	163	16.822	0.021	0.026	1.398	0.00062
	<i>B</i>	162	17.998	0.050	0.038	1.680	1.4×10^{-7}	3.344	0.027 ± 0.005
S5 0153+74	<i>R</i>	136	17.852	0.149	0.040	26.32	0	13.27	0.131 ± 0.009
	<i>B</i>	131	18.324	0.189	0.065	24.52	0	16.11	0.154 ± 0.012
TB 0933+733	<i>R</i>	163	17.334	0.073	0.032	7.83	0	6.10	0.059 ± 0.004
	<i>B</i>	159	17.607	0.075	0.038	8.80	0	6.17	0.056 ± 0.005
HS 1946+7658	<i>R</i>	228	16.429	0.037	0.025	3.08	0	2.60	0.025 ± 0.002
	<i>B</i>	216	17.149	0.059	0.031	4.05	0	4.64	0.045 ± 0.003
S5 2017+74	<i>R</i>	189	18.718	0.094	0.049	6.29	0	7.16	0.067 ± 0.006
	<i>B</i>	182	18.989	0.110	0.049	10.55	0	9.00	0.083 ± 0.006

Notes. No data in Columns (9) and (10) indicate that no significant variability was detected in a light curve. None of the Ly α light curves shows significant variability.

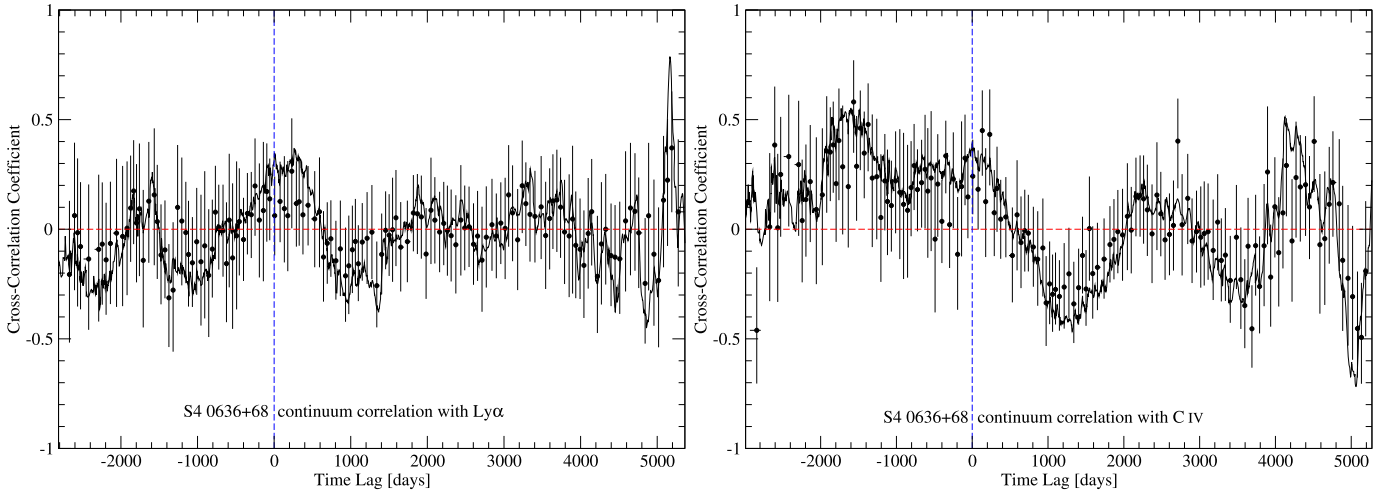
^a N is the number of points in each light curve. The continuum light curve for each object is a merge of the *R*-band light curve and the continuum spectroscopic light curve. The *R* band has a few more points in the light curve than the *B* band because it is somewhat less sensitive when observing through bad weather. Thus, for each object, the number of points in the continuum light curve is slightly larger than the sum of the number of points in the line light curve and the *B*-band light curve.

^b Units are $10^{-16} \text{ erg cm}^{-2} \text{ s}^{-1} \text{ \AA}^{-1}$ for the continuum light curves, $10^{-14} \text{ erg cm}^{-2} \text{ s}^{-1}$ for the emission-line light curves, and apparent magnitude for the *R*-band and *B*-band light curves.

^c Probabilities lower than 10^{-9} are listed as zero.



(a)



(b)

(c)

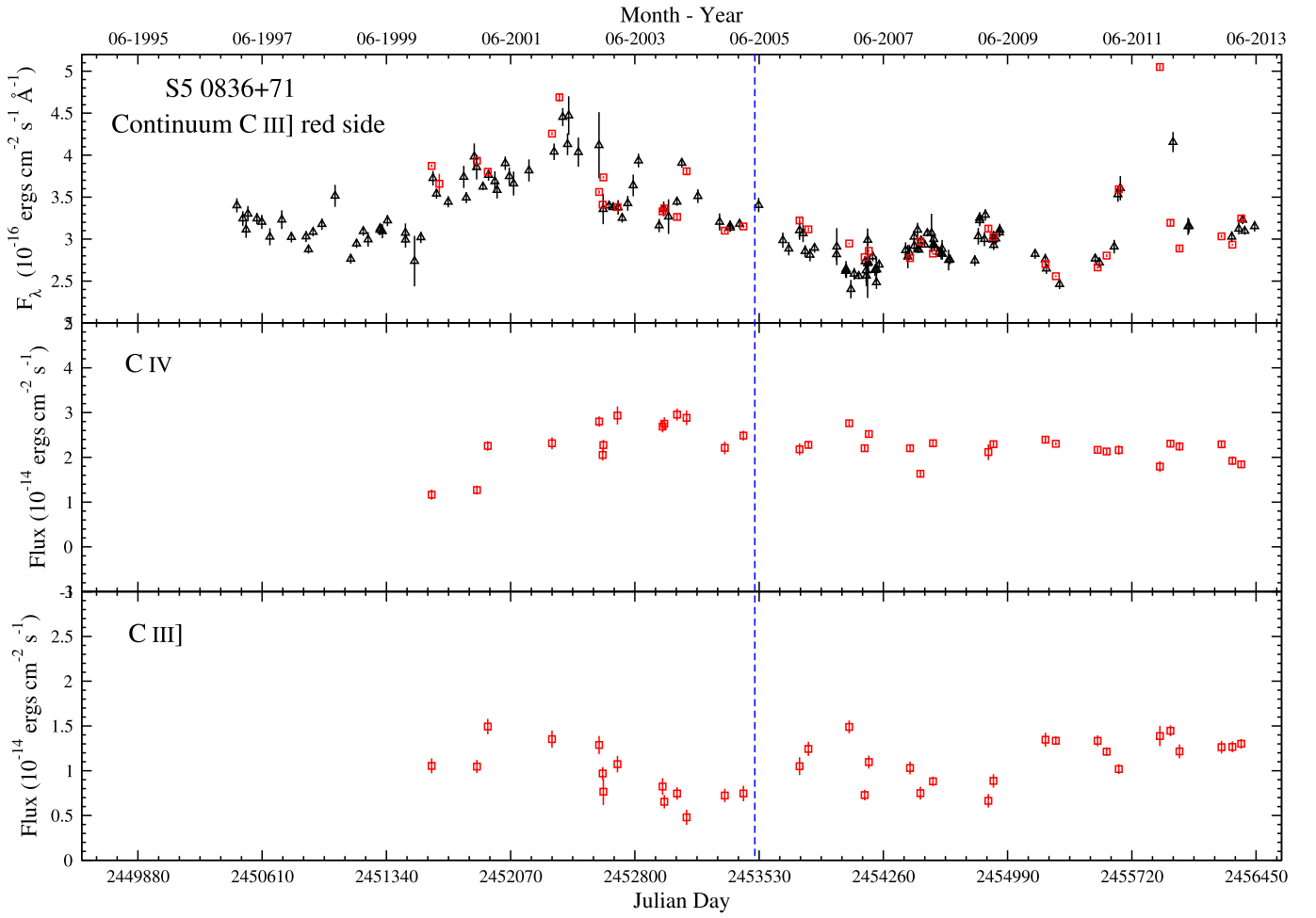
Figure 2. Light curves and CCFs for S 0636+68. (a) Black triangles are photometric data from Wise, and red squares are spectroscopic data from HET. Data up to the vertical dashed blue line were published in Paper I. Panels (b) and (c) show the CCFs for lines as noted in the figure. The time lag is given in the observed frame. ICCF is plotted as the solid line, while ZDCF is plotted as black points with uncertainties. The vertical dashed blue line denotes a time lag of zero, and the horizontal dashed red line denotes a cross-correlation coefficient of zero. No significant peak is identified in either of the CCFs.

3.3.1. S4 0636+68

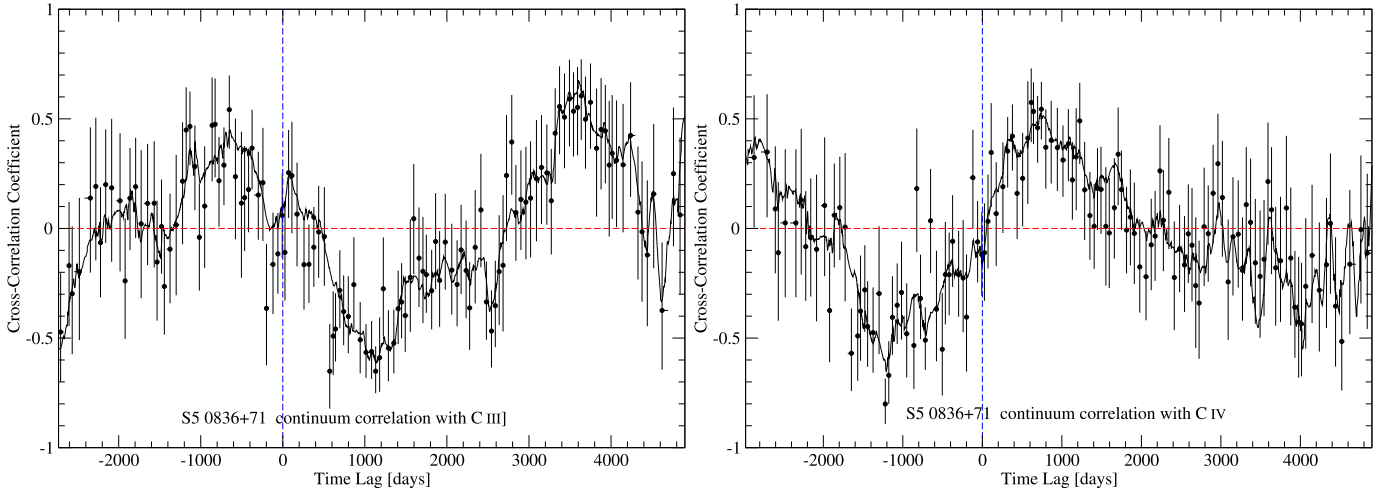
No time lag is detected in the two emission lines that we monitored, Ly α and C IV.

3.3.2. S5 0836+71

A C IV time lag of 188^{+27}_{-37} days in the quasar rest frame was detected in this object, as we previously reported in Paper I.



(a)



(b)

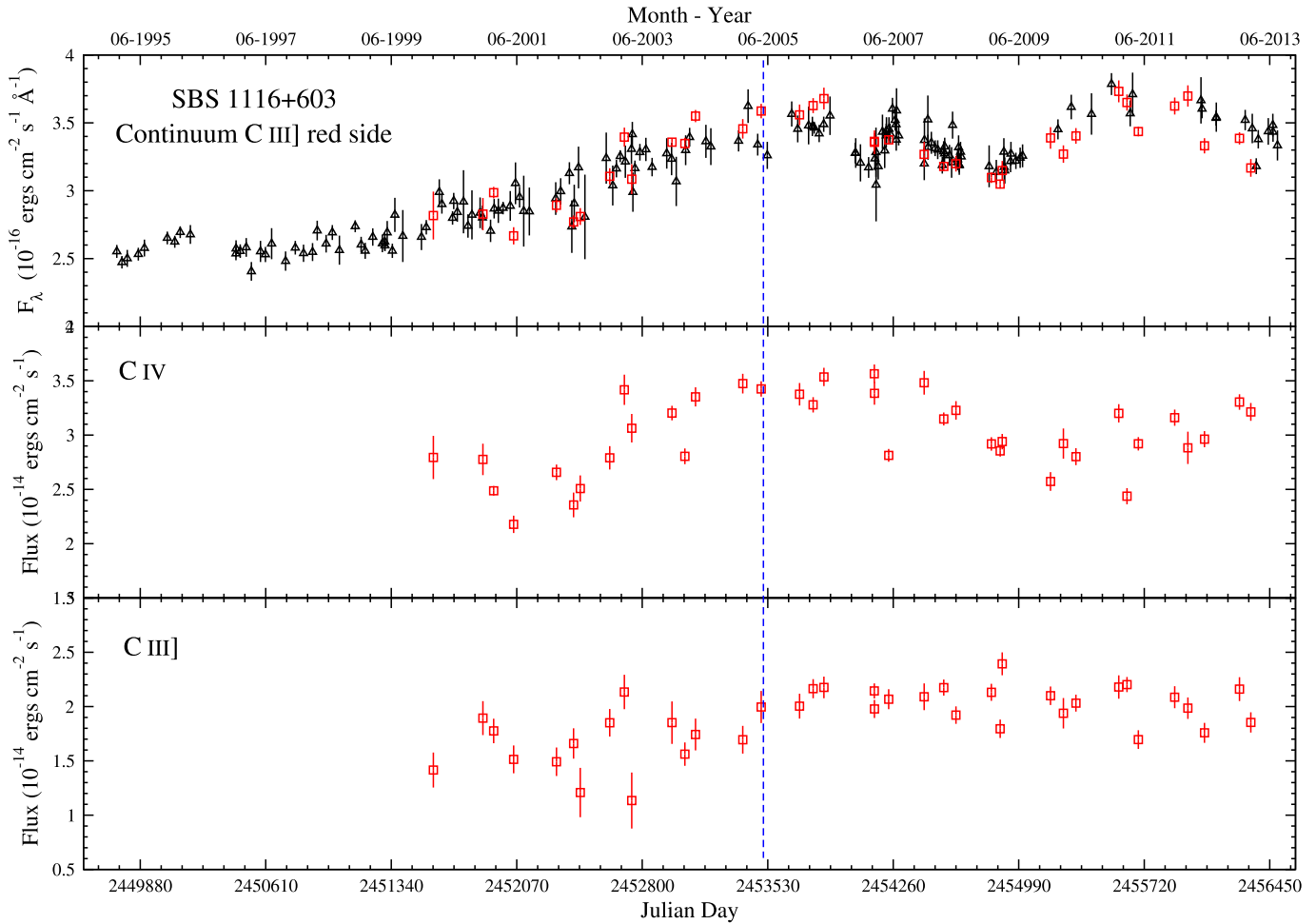
(c)

Figure 3. Light curves and CCFs for S5 0836+71. Symbols as in Figure 2. (b) The peak seen in the C III] CCF, at ~ 3600 days, is marginally significant. See text for discussion. (c) A significant time lag is detected for the C IV line.

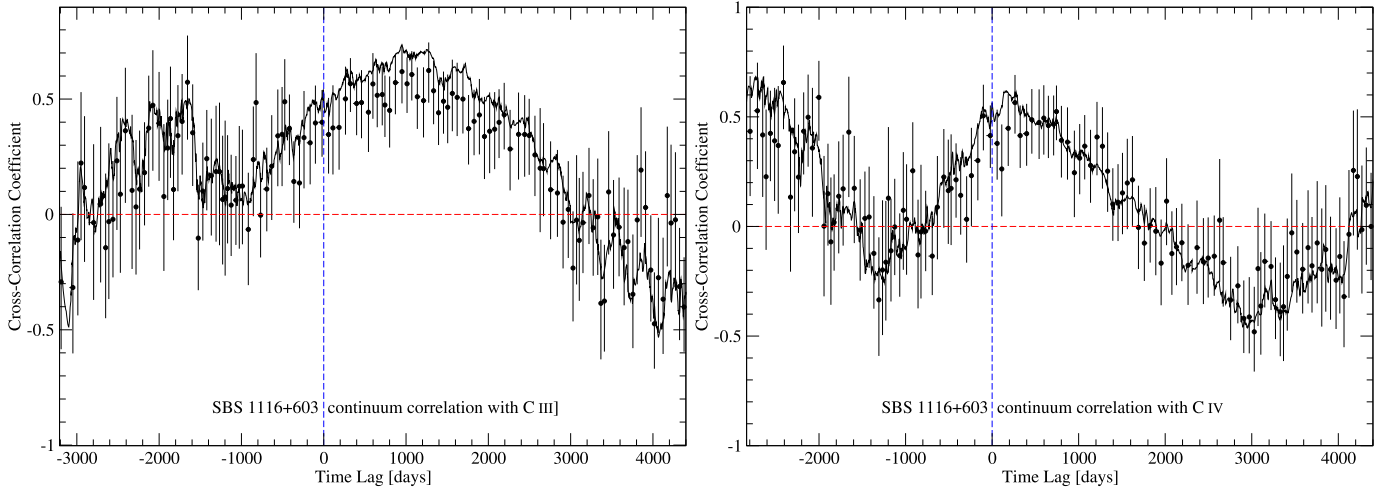
The current result is consistent with the result we preliminarily found a decade ago when we had only about half the data we are reporting in this work.

The CCF of C III] with the continuum in S5 0836+71 shows a time lag of about 3570 ± 140 days in the observed frame. Although formally significant, we note that this time lag is a

result of the cross correlation of the first three years of the continuum light curve with the last three years of the C III] light curve. This is too brief an overlap interval to significantly detect such a large time lag, and we do not claim this detection as significant. This was also not detected in Paper I due to the shorter monitoring period reported there.



(a)



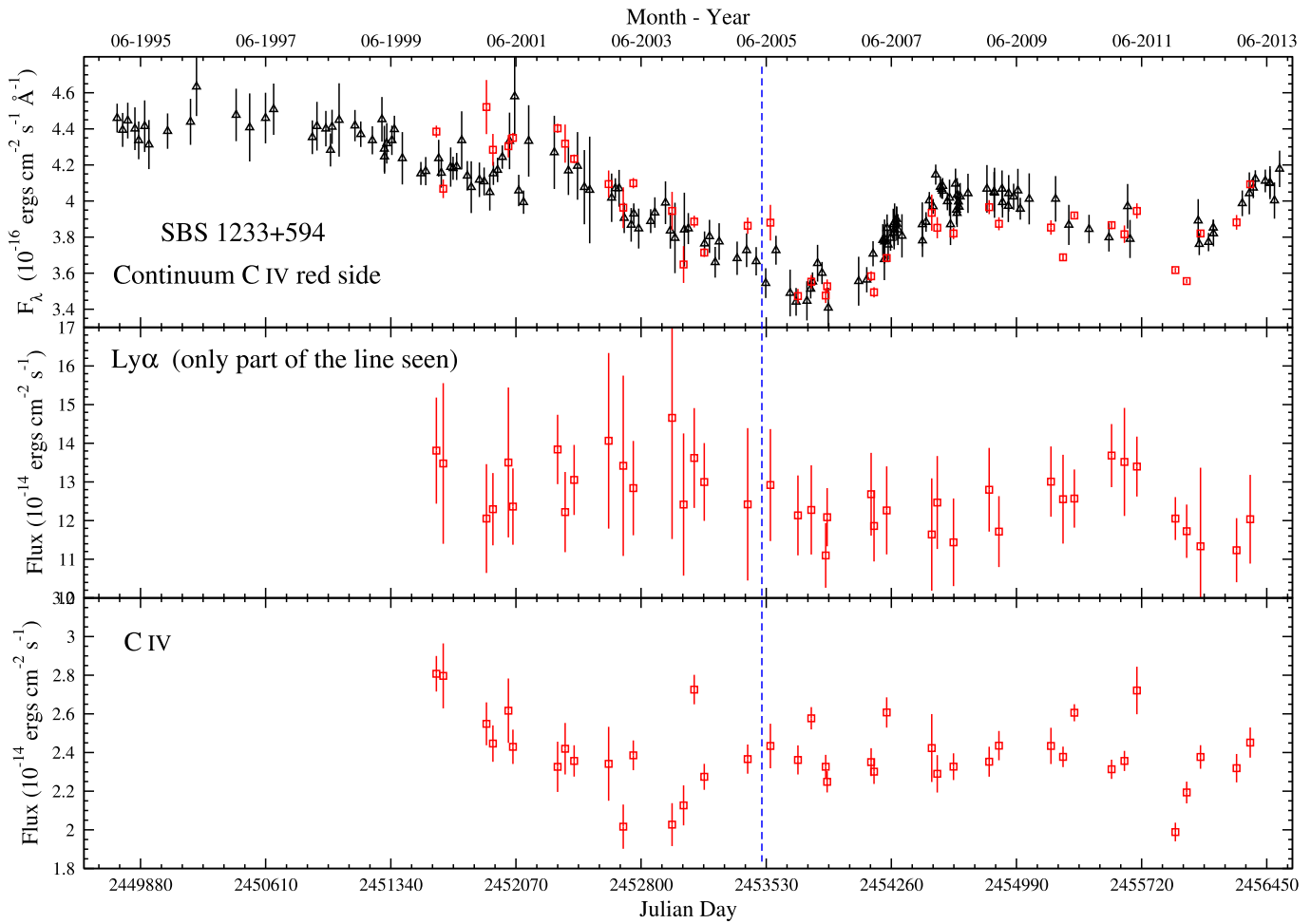
(b)

(c)

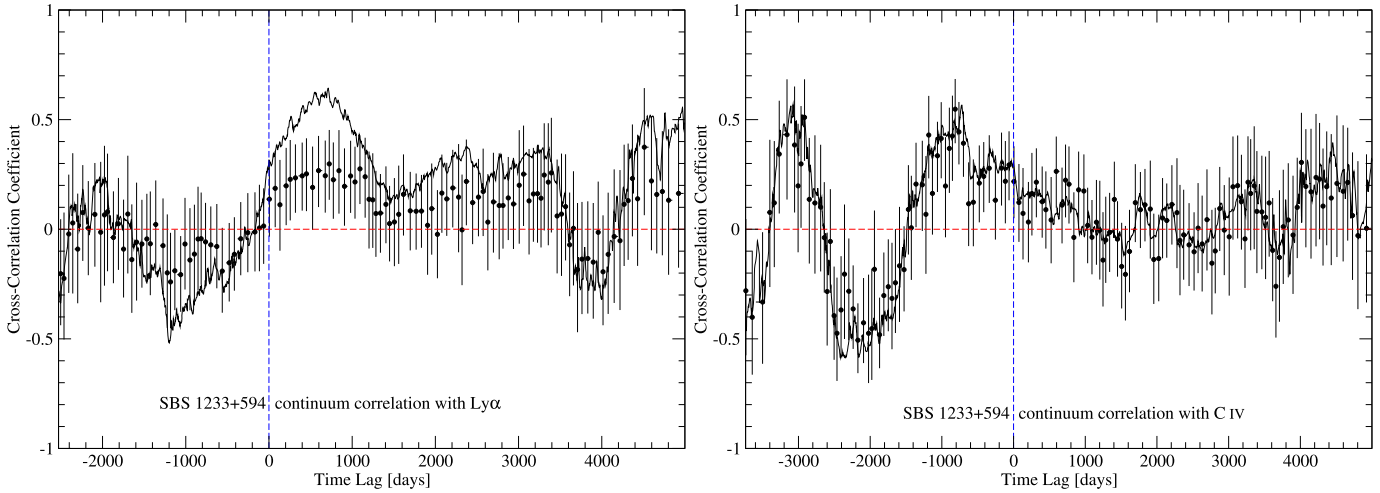
Figure 4. Light curves and CCFs for SBS 1116+603. Symbols as in Figure 2. Panels (b) and (c) Both CCFs show significant peaks.

Jorstad et al. (2013) reported an increase in the γ -ray activity of S5 0836+71 in March 2011 based on Fermi observations that lasted for a year. They also report a sharp γ -ray flare at the end of 2011, which was also accompanied by an increase in the optical brightness of the quasar by ~ 0.5 mag in the R band. This is in accord with the light curve we

present in Figure 3, which shows this flare at the same time. No other strong flares like this are seen in our light curves. Our result is not sensitive to this flare because it occurred about two years before the end of our campaign, and any response to this continuum flare in the lines would be after the end of our observations.



(a)



(b)

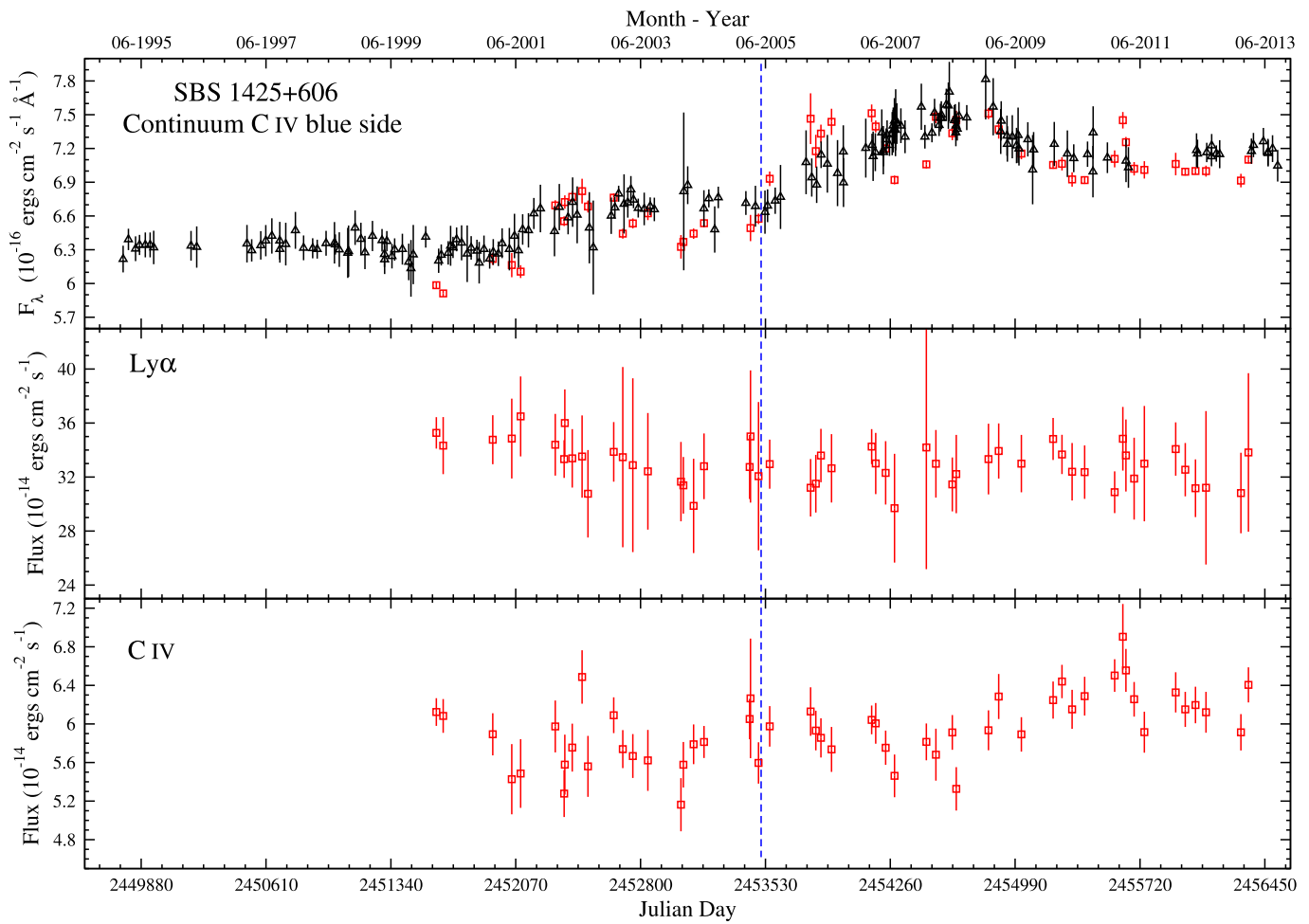
(c)

Figure 5. Light curves and CCFs for SBS 1233+594. Symbols as in Figure 2. Panel (b) Although the ICCF for the Ly α line shows a significant peak, the ZDCF method does not show this peak. See text for discussion. Panel (c) No significant time lag is detected for the C IV line.

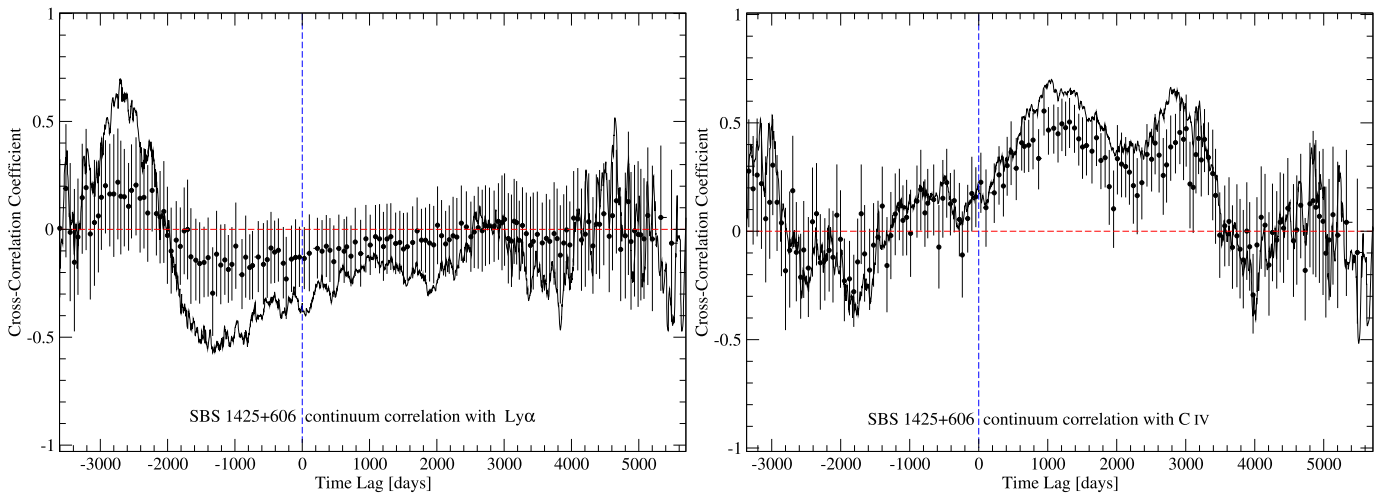
3.3.3. SBS 1116+603

A C IV time lag was detected for this object, although this was not detected in Paper I, probably due to the shorter monitoring period and because there was no significant variability feature in the light curve in that period.

A C III] time lag was also detected in this object, and it is found to be 262^{+72}_{-72} days in the rest frame. This is the only object for which we detected a significant C III] time lag out of the three objects in which we monitored that line.



(a)



(b)

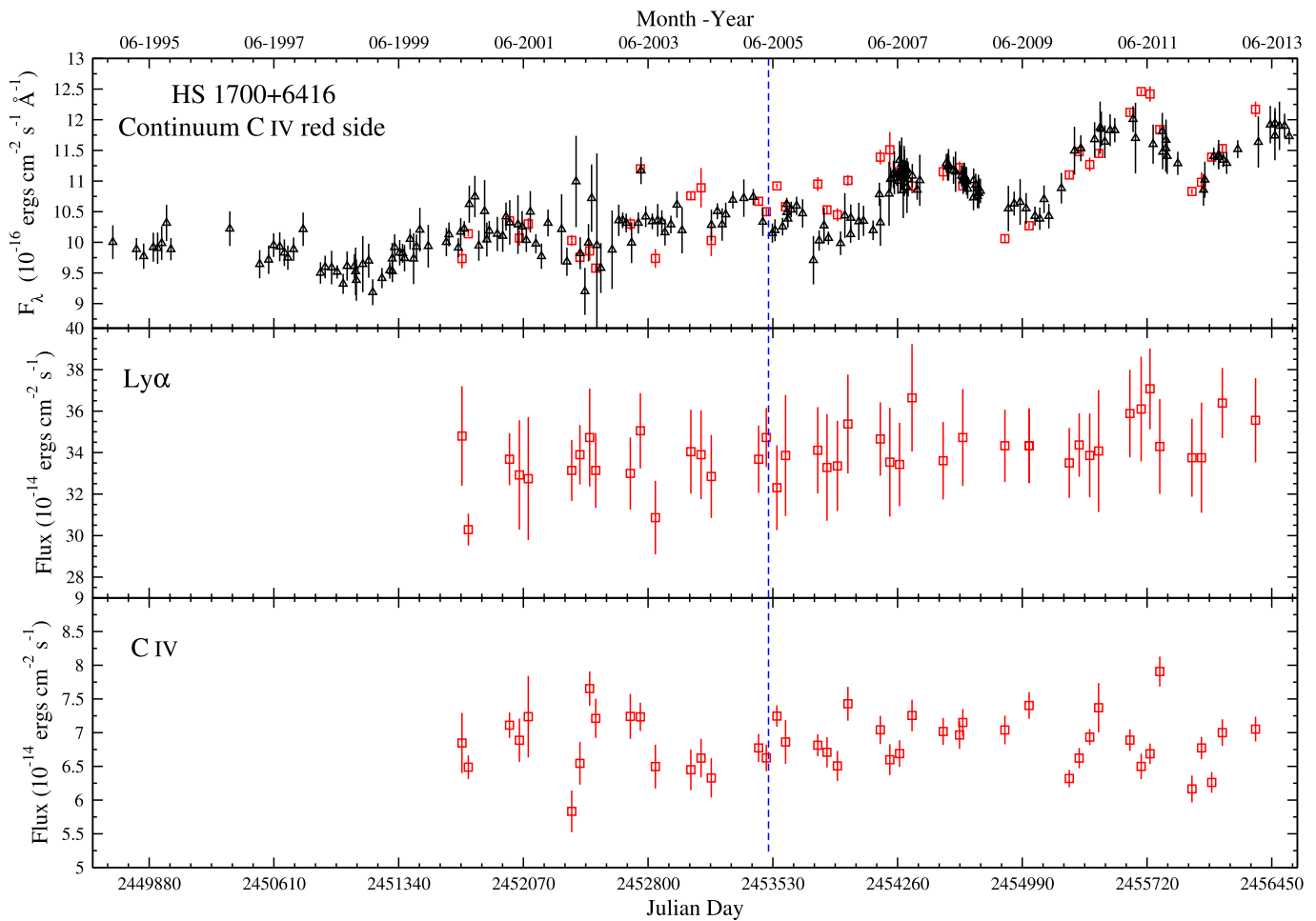
(c)

Figure 6. Light curves and CCFs for SBS 1425+606. Symbols as in Figure 2. Panel (b) No significant time lag is detected in the Ly α line. Panel (c) A significant time lag is detected for the C IV line.

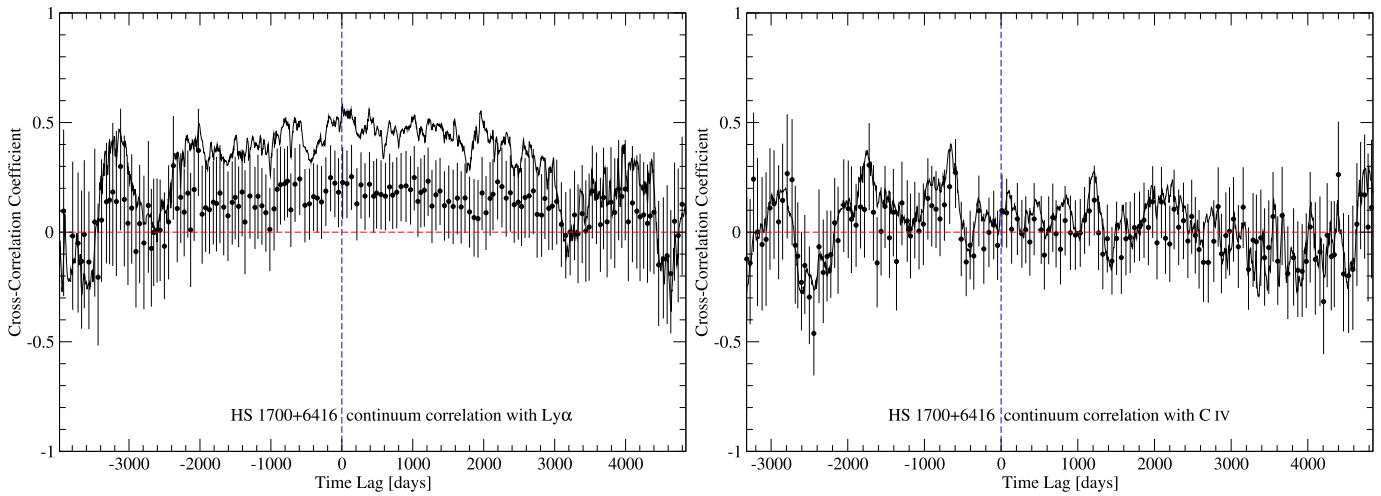
3.3.4. SBS 1233+594

There is a hint of a Ly α time lag in the ICCF at about 165 days in the rest frame. However, this peak is not detected with

the ZDCF method, and using the FR/RSS method, the lag is consistent with zero. We therefore exclude this result from further discussion. For the second line monitored in this object, C IV, no time lag was detected.



(a)



(b)

(c)

Figure 7. Light curves and CCFs for HS 1700+6416. Symbols as in Figure 2. Panels (b) and (c) No significant peak is identified in either of the CCFs.

3.3.5. SBS 1425+606

A C IV time lag is detected, but no Ly α time lag. In Paper I no time lag was detected for this object as the continuum light curve in the first 10 yr of the monitoring shows only a gradual rise, and a shorter-timescale feature of luminosity increase and decrease was detected only in the last eight years of monitoring.

3.3.6. HS 1700+6416

Even though the continuum light curve shows variability and features of higher and lower luminosity, no line variations are detected in response to these continuum changes in the two emission lines that we monitored, Ly α and C IV.

Table 4
Continuum Light Curves

JD	f_{λ}^a
S4 0636+68	
2449667.42	6.340 ± 0.147
2449728.43	6.396 ± 0.172
2449773.24	6.285 ± 0.157
2449804.22	6.285 ± 0.140
2449954.56	6.128 ± 0.193
2449981.58	6.068 ± 0.152
2450007.50	5.672 ± 0.173
2450035.48	5.831 ± 0.167
2450080.23	5.812 ± 0.140
2450104.38	5.864 ± 0.147

Note. Table 4 is presented in its entirety in the electronic edition of the Astrophysical Journal. A portion is shown here for guidance regarding its form and content.

^a In units of 10^{-16} erg cm⁻² s⁻¹ Å⁻¹.

(This table is available in its entirety in machine-readable form.)

Table 5
Line Light Curves

JD	f_{λ}^a
S4 0636+68—Ly α	
2451871.93	11.553 ± 0.496
2451935.69	11.727 ± 1.093
2452337.66	11.508 ± 0.886
2452559.99	11.790 ± 0.816
2452618.84	11.872 ± 0.722
2452698.65	12.013 ± 1.659
2452962.88	12.577 ± 0.953
2452970.87	12.380 ± 0.656
2453047.68	13.282 ± 0.343
2453294.97	12.770 ± 0.542

Note. Table 5 is presented in its entirety in the electronic edition of the Astrophysical Journal. A portion is shown here for guidance regarding its form and content.

^a In units of 10^{-14} erg cm⁻² s⁻¹.

(This table is available in its entirety in machine-readable form.)

3.3.7. Summary

We found line time lags for three out of the six monitored objects. Two of these AGNs are radio loud and one is radio quiet (see Table 1). In Paper I we reported preliminary results from the first 5 yr of monitoring, including one preliminary time-lag measurement. No other lines showed statistically significant time lags in the first 5 yr of monitoring. In this paper we find that after adding eight more years to make a total of 13 yr of spectrophotometric monitoring, we can measure time lags for three of the six objects. This supports the idea that a monitoring period of more than a decade is needed in order to carry out a successful RM campaign on quasars at the high end of the luminosity range.

Half of the objects in our sample are radio loud, and their continuum luminosity variability may be affected not only by the central accretion disk, as is assumed in RM, but also by the jet. Several studies (e.g., León-Tavares et al. 2013; Paltani & Türler 2003) found evidence for components of the BLR that respond to jet flares seen in gamma-ray energies. However, the

gamma-ray flares and the response seen in emission lines such as Mg II, H α , and H β , are on short timescales of days to weeks, and our current study is not sensitive to these timescales due to our cadence of more than a month. Thus, the effect of possible jet flares on our time-lag results are negligible and probably well within our reported uncertainties.

We measured the rest-frame equivalent width of the lines in our spectra to be 10 Å to 20 Å for the C IV emission line and between 50 Å and 100 Å for the Ly α emission line. These values are in accord with other high-redshift high-luminosity AGNs (e.g., Constantin et al. 2002; Dietrich et al. 2002). This indicates that there is no large optical dilution by a beamed jet optical continuum in these sources (e.g., Shaw et al. 2012).

Due to the small number of objects in our campaign and the small number of time lags that are detected, it is hard to find a way to estimate the number of false detections in our study, which suffers from very small number statistics. A basic way to estimate the number of false detections is to look at the number of peaks on the negative side of the CCFs that could be declared as significant time lags.¹² A careful inspection of our 12 CCFs yields that if using the criteria to define a peak when it appears clearly both in the ICCF and ZDCF and has a peak coefficient above 0.5, then no feature on the negative side of the CCF can be defined as a significant peak. This reinforces our detected positive lags as being true detections.

4. Discussion

4.1. C IV BLR Size–Luminosity Relation

In Table 6 we list the three objects for which we have found significant and reliable C IV reverberation lags. To these we add a compilation of previous measurements, including C IV BLR sizes for a few Seyfert AGNs that were reanalyzed and compiled by Peterson et al. (2004, 2005), Metzroth et al. (2006), and De Rosa et al. (2015). Lira et al. (2018) reported time lags for eight high-luminosity quasars, but with a number of mistakes that were corrected in a recent erratum (e.g., a few incorrect rest-frame time lags and their uncertainties in their Table 4 and mismatched objects in their Figure 7); these mistakes were only in the presentation and did not affect their final analysis. The numbers in Table 6 include all the corrections to the Lira et al. (2018) measurements. We also include in Table 6 the two quasars reported by Hoormann et al. (2019), the 16 objects that are the “gold sample” of Grier et al. (2019), and the three objects from Shen et al. (2019). Figure 9 displays the 38 objects from Table 6 with reliable and significant C IV time-lag measurements.

Linear regression for the C IV BLR size–luminosity relation is performed with the two methods detailed in Kaspi et al. (2005, 2007): (1) the FITEXY approach of Press et al. (1992) with the Tremaine et al. (2002) procedure to account for the intrinsic scatter in the data, and (2) the bivariate correlated errors and intrinsic scatter (BCES) regression method (Akritas & Bershady 1996). The two techniques take into account the uncertainty in the BLR size, the luminosity, and the intrinsic scatter around a straight line. The fit from the FITEXY method

¹² As defined in Section 3.2, we consider a time lag as significant if the CCF possesses a maximum with a peak correlation larger than 0.5 in both the ICCF and ZDCF, and that it is a result of a significant overlap of the continuum and line light curves.

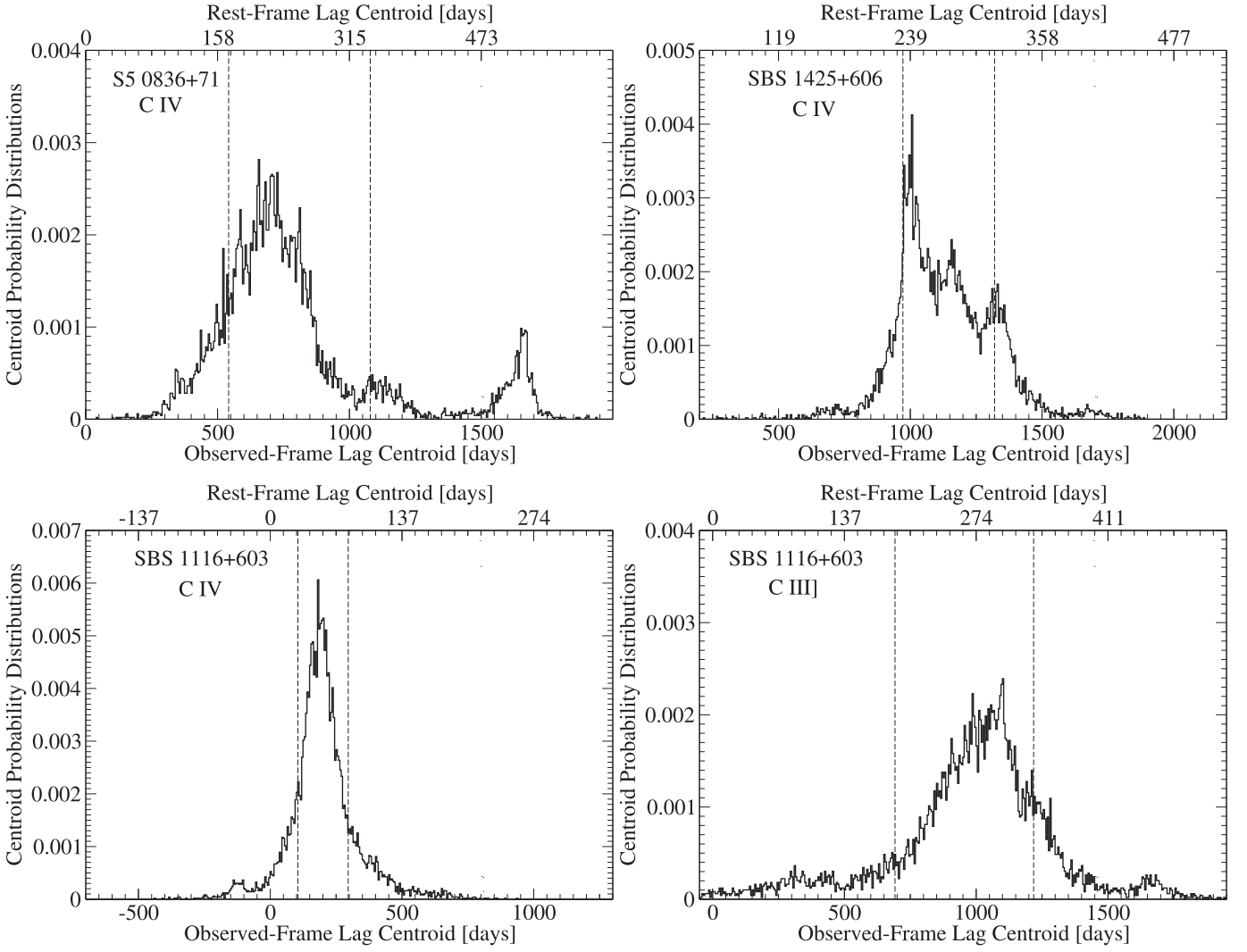


Figure 8. CCCDs for the four significant time lags found in this paper. The lag centroid is given in days in the observed frame and in the rest frame. The dashed vertical lines encompass the range that includes 68% of the Monte Carlo realizations. This range determines the uncertainty on the time-lag from the ICCF (Peterson et al. 1998).

(solid line in Figure 9) is

$$\frac{R_{\text{BLR}}}{10 \text{ lt days}} = (0.25 \pm 0.05) \left(\frac{\lambda L_{\lambda}(1350 \text{ \AA})}{10^{43} \text{ erg s}^{-1}} \right)^{0.45 \pm 0.03}, \quad (1)$$

and for the BCES method (dashed line in Figure 9), it is

$$\frac{R_{\text{BLR}}}{10 \text{ lt days}} = (0.34 \pm 0.11) \left(\frac{\lambda L_{\lambda}(1350 \text{ \AA})}{10^{43} \text{ erg s}^{-1}} \right)^{0.45 \pm 0.05}. \quad (2)$$

For these data the Pearson correlation coefficient is 0.90 with a significance level of 4×10^{-13} , and the Spearman rank-order correlation is 0.80, with a significance level of 1×10^{-10} . The intrinsic scatter using the Tremaine et al. (2002) procedure is 58%. These results are similar to those found by Lira et al. (2018; a slope of 0.46 ± 0.08 and a constant of 0.22 ± 0.10) and are in accord with the preliminary results reported in Kaspi et al. (2007). The uncertainties are about half of these reported by Lira et al. (2018). Our slope is also consistent within the uncertainties with that measured by Grier et al. (2019), who find a slope of 0.51 ± 0.05 for their full sample and a slope of 0.52 ± 0.04 for their gold sample.

Almost all objects in Figure 9 lie in the range of $10^{43} \lesssim \lambda L_{\lambda}(1350 \text{ \AA}) \lesssim 10^{48} \text{ erg s}^{-1}$, i.e., covering five orders of magnitudes in luminosity. There is one object three orders of magnitudes below this range: NGC 4395 at $\lambda L_{\lambda}(1350 \text{ \AA}) \approx 10^{40} \text{ erg s}^{-1}$. Thus, this one object may significantly affect the BLR size–luminosity relation through its statistical leverage. Repeating the fit without NGC 4395 in the sample, we find a slope of 0.40 ± 0.04 using the FITEXY method and 0.38 ± 0.05 using the BCES method. This may indicate that the true relation has a shallower slope than the theoretically predicted slope of 0.5, although further reverberation studies on lower-luminosity AGNs are needed in order to better understand this issue.

We have found a significant C IV time lag for three out of our six spectroscopically monitored quasars, i.e., in 50% of the objects studied. This success rate is comparable to that of Lira et al. (2018), who found C IV time lags for 8 out of their 17 monitored quasars. In contrast, while Lira et al. (2018) also found Ly α time lags in 50% of their objects, we have found only a hint of a Ly α time lag in one of our objects. This is probably because in two of our objects only part of the Ly α line is within the spectral range covered, in one it is outside the

Table 6
C IV Data

Object	$\lambda L_{\lambda}(1350 \text{ \AA})$ erg s ⁻¹	Time Lag ^a days	Reference	Redshift	FWHM ^a km s ⁻¹	log M_{BH} log M_{\odot}
(1)	(2)	(3)	(4)	(5)	(6)	(7)
NGC 4395	$(8.15 \pm 0.51) \times 10^{39}$	$0.040^{+0.024}_{-0.018}$	Peterson et al. (2005)	0.001064	3100 ± 1000	$4.73^{+0.45}_{-0.61}$
NGC 3783	$(3.89 \pm 0.81) \times 10^{43}$	$3.8^{+1.0}_{-0.9}$	Peterson et al. (2005)	0.00973	3690 ± 480	$6.88^{+0.21}_{-0.24}$
NGC 7469	$(6.03 \pm 0.98) \times 10^{43}$	$2.5^{+0.3}_{-0.2}$	Peterson et al. (2005)	0.01632	4310 ± 420	$6.83^{+0.13}_{-0.13}$
3C 390.3	$(1.18 \pm 0.59) \times 10^{44}$	$35.7^{+11.4}_{-14.6}$	Peterson et al. (2005)	0.0561	9700 ± 1700	$8.69^{+0.26}_{-0.39}$
NGC 4151	$(4.28 \pm 1.27) \times 10^{42}$	$3.34^{+0.82}_{-0.77}$	Metzroth et al. (2006)	0.00332	5780 ± 920	$7.21^{+0.22}_{-0.26}$
NGC 5548	$(3.89 \pm 0.79) \times 10^{43}$	$4.53^{+0.35}_{-0.34}$	De Rosa et al. (2015)	0.01676	6710 ± 490	$7.48^{+0.09}_{-0.10}$
CTS 286	$(11.16 \pm 1.83) \times 10^{46}$	459^{+71}_{-92}	Lira et al. (2018)	2.551	6260 ± 630	$9.42^{+0.15}_{-0.19}$
CTS 406	$(8.13 \pm 0.75) \times 10^{46}$	98^{+55}_{-74}	Lira et al. (2018)	3.178	6240 ± 620	$8.75^{+0.28}_{-0.70}$
CTS 564	$(9.95 \pm 1.51) \times 10^{46}$	115^{+184}_{-29}	Lira et al. (2018)	2.653	5620 ± 560	$8.73^{+0.50}_{-0.22}$
CTS 650	$(7.59 \pm 1.83) \times 10^{46}$	162^{+33}_{-10}	Lira et al. (2018)	2.659	3420 ± 340	$8.44^{+0.16}_{-0.12}$
CTS 953	$(9.99 \pm 1.97) \times 10^{46}$	73^{+15}_{-58}	Lira et al. (2018)	2.526	5000 ± 500	$8.43^{+0.49}_{-0.78}$
CTS 1061	$(33.88 \pm 3.15) \times 10^{46}$	91^{+111}_{-24}	Lira et al. (2018)	3.368	3220 ± 320	$8.14^{+0.43}_{-0.22}$
J 214355	$(9.17 \pm 1.02) \times 10^{46}$	136^{+100}_{-90}	Lira et al. (2018)	2.607	6900 ± 690	$8.98^{+0.32}_{-0.56}$
J 221516	$(14.29 \pm 1.86) \times 10^{46}$	153^{+91}_{-12}	Lira et al. (2018)	2.709	5890 ± 590	$8.89^{+0.29}_{-0.13}$
DES J0228-04	$(2.69 \pm 0.25) \times 10^{46}$	123^{+43}_{-42}	Hoormann et al. (2019)	1.905	7800 ± 1700	$9.04^{+0.30}_{-0.40}$
DES J0033-42	$(3.24 \pm 0.15) \times 10^{46}$	95^{+16}_{-23}	Hoormann et al. (2019)	2.593	7700 ± 650	$8.92^{+0.14}_{-0.20}$
RMID 032	$(3.11 \pm 0.15) \times 10^{44}$	$21.1^{+22.7}_{-8.3}$	Grier et al. (2019)	1.715	5010 ± 20	$7.89^{+0.32}_{-0.22}$
RMID 052	$(3.155 \pm 0.015) \times 10^{45}$	$32.6^{+6.9}_{-2.1}$	Grier et al. (2019)	2.305	3354 ± 67	$7.73^{+0.10}_{-0.05}$
RMID 181	$(3.508 \pm 0.12) \times 10^{44}$	$102.1^{+26.8}_{-10.0}$	Grier et al. (2019)	1.675	4533 ± 49	$8.49^{+0.11}_{-0.05}$
RMID 249	$(9.64 \pm 0.22) \times 10^{44}$	$22.8^{+31.3}_{-11.5}$	Grier et al. (2019)	1.717	2601 ± 29	$7.35^{+0.38}_{-0.31}$
RMID 256	$(1.2270 \pm 0.0085) \times 10^{45}$	$43.1^{+49.0}_{-13.1}$	Grier et al. (2019)	2.244	3565 ± 9	$7.90^{+0.34}_{-0.20}$
RMID 275	$(4.0830 \pm 0.0094) \times 10^{45}$	$76.7^{+10.0}_{-3.9}$	Grier et al. (2019)	1.577	6943 ± 22	$8.73^{+0.06}_{-0.03}$
RMID 298	$(3.9450 \pm 0.0091) \times 10^{45}$	$82.3^{+64.5}_{-24.5}$	Grier et al. (2019)	1.635	5177 ± 51	$8.51^{+0.26}_{-0.16}$
RMID 312	$(1.194 \pm 0.011) \times 10^{45}$	$70.9^{+9.6}_{-3.3}$	Grier et al. (2019)	1.924	10248 ± 53	$9.04^{+0.06}_{-0.03}$
RMID 332	$(3.556 \pm 0.016) \times 10^{45}$	$83.8^{+23.3}_{-6.5}$	Grier et al. (2019)	2.581	7828 ± 32	$8.88^{+0.11}_{-0.04}$
RMID 387	$(4.864 \pm 0.011) \times 10^{45}$	$48.4^{+34.7}_{-10.1}$	Grier et al. (2019)	2.426	4797 ± 30	$8.21^{+0.24}_{-0.11}$
RMID 401	$(3.090 \pm 0.021) \times 10^{45}$	$60.6^{+36.7}_{-13.0}$	Grier et al. (2019)	1.822	10120 ± 497	$8.96^{+0.25}_{-0.15}$
RMID 418	$(1.0960 \pm 0.0076) \times 10^{45}$	$58.6^{+31.6}_{-21.3}$	Grier et al. (2019)	1.418	6159 ± 44	$8.51^{+0.28}_{-0.20}$
RMID 470	$(6.622 \pm 0.092) \times 10^{44}$	$27.4^{+53.5}_{-22.0}$	Grier et al. (2019)	1.879	5028 ± 70	$8.01^{+0.53}_{-0.72}$
RMID 527	$(6.138 \pm 0.042) \times 10^{44}$	$47.3^{+13.3}_{-5.0}$	Grier et al. (2019)	1.647	8306 ± 53	$8.68^{+0.11}_{-0.05}$
RMID 549	$(2.339 \pm 0.011) \times 10^{45}$	$68.9^{+31.6}_{-9.6}$	Grier et al. (2019)	2.275	4995 ± 53	$8.40^{+0.17}_{-0.07}$
RMID 734	$(3.3880 \pm 0.0078) \times 10^{45}$	$68.0^{+38.2}_{-11.5}$	Grier et al. (2019)	2.332	7042 ± 65	$8.69^{+0.20}_{-0.09}$
RMID 363	$(3.16 \pm 0.15) \times 10^{46}$	$300.4^{+17.1}_{-4.7}$	Shen et al. (2019)	2.635	$5252 \pm 94^{\text{b}}$	$9.08^{+0.04}_{-0.02}$
RMID 372	$(4.17 \pm 0.19) \times 10^{45}$	$67.0^{+20.4}_{-7.4}$	Shen et al. (2019)	1.745	$10451 \pm 68^{\text{b}}$	$9.03^{+0.12}_{-0.06}$
RMID 651	$(2.63 \pm 0.12) \times 10^{45}$	$91.7^{+56.3}_{-22.7}$	Shen et al. (2019)	1.486	$6391 \pm 52^{\text{b}}$	$8.74^{+0.21}_{-0.13}$
S5 0836+71	$(1.03 \pm 0.16) \times 10^{47}$	230^{+91}_{-59}	This work	2.172	9000 ± 800	$9.44^{+0.22}_{-0.21}$
SBS 1116+603	$(1.80 \pm 0.20) \times 10^{47}$	65^{+17}_{-37}	This work	2.646	4800 ± 450	$8.34^{+0.18}_{-0.45}$
SBS 1425+606	$(4.52 \pm 0.37) \times 10^{47}$	285^{+30}_{-53}	This work	3.192	8200 ± 470	$9.45^{+0.09}_{-0.14}$

Notes.^a In the rest frame.^b Computed from the measured σ_{line} using the line profile Gaussian assumption: $\text{FWHM} = 2.355 \times \sigma_{\text{line}}$.

range, and in the other two cases, the light curve is too noisy due to low signal-to-noise ratio at the blue end of the spectrum and the many absorption lines from the Ly α forest. We measure one significant C III] time lag, as did Lira et al. (2018). This line is much weaker than C IV, and hence its light curves are noisy and challenging for time-lag detection.

All six AGNs in our spectrophotometrically monitored sample show significant 1350 Å continuum variations at the level of 20%–70%. However, we detect corresponding C IV variations only in half of the them. This is similar to Lira et al. (2018), who also do not find corresponding variations in the C IV light curves of about half of their AGNs sample, in spite of significant variations in their continuum light curves. This may suggest that the ionizing continuum in high-luminosity AGNs

behaves differently from the 1350 Å continuum and that this different behavior is a common phenomenon in these objects.

Comparing the H β BLR size to the C IV BLR size is important to constrain BLR models that aim to produce the BLR emission lines (e.g., Netzer 2020). The calculated BLR models predict that the C IV BLR size is about half the H β BLR size. Using the measured relation of H β BLR size and the luminosity $\lambda L_{\lambda}(5100 \text{ \AA})$ of the entire sample in Equation (5) of Du et al. (2015) and the estimated $\lambda L_{\lambda}(5100 \text{ \AA})$ of the objects in our sample (Table 1)¹³, we can estimate the H β BLR size for the three objects in which we measured the C IV BLR size. We

¹³ Note that these $\lambda L_{\lambda}(5100 \text{ \AA})$ estimates are based on our measured $\lambda L_{\lambda}(1350 \text{ \AA})$ and thus they are not independent measurements.

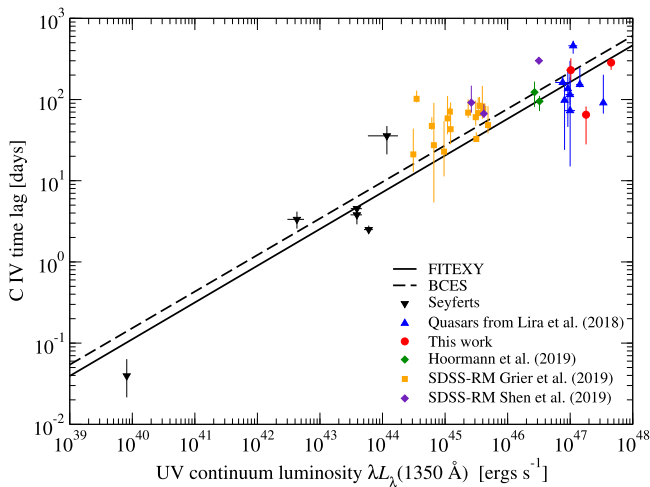


Figure 9. C IV BLR size–UV luminosity relation. Time lag is in the quasar rest frame.

find $H\beta$ BLR sizes of 650_{-160}^{+210} light days for S5 08036+71, 855_{-220}^{+295} light days for SBS 1116+603, and 1360_{-380}^{+520} light days for SBS 1425+606. The ratio of these sizes and the C IV BLR sizes measured in this work shows a large scatter between 3 to 13. This is mainly due to the exceptionally small C IV BLR size that we measured in SBS 1116+603. Moreover, we use only three objects and not a larger sample. This does not enable proper statistics with small standard deviation. Thus, in order to compare the $H\beta$ and C IV BLR sizes, it is better to use the mean relations. We therefore compare the mean relation between the C IV BLR size and $\lambda L_{\lambda}(1350 \text{ \AA})$, which we find in Equation (1) to the mean relation between the $H\beta$ BLR size and $\lambda L_{\lambda}(5100 \text{ \AA})$ from Du et al. (2015). Using these averaged measured BLR sizes, we find that for $\lambda L_{\lambda}(5100 \text{ \AA}) = 10^{45} \text{ erg s}^{-1}$, the ratio of the $H\beta$ to C IV BLR sizes is 3.3, while for $\lambda L_{\lambda}(5100 \text{ \AA}) = 10^{47} \text{ erg s}^{-1}$, this factor is 4.1. This is larger than previously predicted by BLR models, and thus a change in the models (Netzer 2020) may be needed in order to fit the observations.

4.2. Mass–Luminosity Relation

Assuming gravitationally dominated motions of the BLR clouds, the central masses of AGNs can be estimated using $M_{\text{BH}} = fG^{-1}V^2r$, where V is an estimate of the velocity of the BLR around the central mass, and r is an estimate of the typical distance between the BLR gas and the central BH. f is a scaling factor that embodies our ignorance of the BLR geometry and velocity field (e.g., Peterson et al. 2004). This method for estimating M_{BH} has been widely used over the past two decades, with various choices for f and for the observational indicator of v , mainly for BLR distances determined from RM of the $H\beta$ emission line.

Although several attempts have been made to estimate M_{BH} from C IV emission-line reverberation (e.g., Vestergaard & Peterson 2006; Park et al. 2013), it was found that this line has several drawbacks. The width of the C IV line is weakly correlated with the width of low-ionization lines such as $H\beta$ and Mg II. The C IV profiles also often show high blueshifts and asymmetries that indicate nonvirial motions (e.g., Baskin & Laor 2005; Netzer et al. 2007; Shang et al. 2007; Richards et al. 2011; Trakhtenbrot & Netzer 2012). Coatman et al. (2017) used a sample of 230 quasars to quantify the bias in C IV BH

masses as a function of the C IV blueshift and suggested an empirical formula to derive the BH mass from the C IV emission-line properties. On the other hand, Mejía-Restrepo et al. (2018) further studied the possibility that C IV can serve for BH mass estimates from a single-epoch spectrum by using three different methods to improve the measurement. They find these methods to be of limited applicability, mostly because they depend on correlations that are driven by the line width of the C IV profile and not by an interconnection between the line width of the C IV line and the line width of the low-ionization lines. The conclusion of Mejía-Restrepo et al. (2018) is that C IV-based mass estimates at high redshift cannot serve as an alternative for estimates based on low-ionization lines such as $H\alpha$, $H\beta$, and Mg II.

Mejía-Restrepo et al. (2016) used a sample of 39 AGNs at $z \sim 1.55$ that have measurements of both the $H\beta$ and C IV emission lines to measure the BH mass from the two lines. In addition, Vietri et al. (2020) used a sample of 21 AGN at $z \sim 2$ with measurements of these two lines to derive the BH masses from the two lines. In both studies the agreement between the derived masses from the two lines is poor, and this confirms the inconsistency of mass estimates based on the C IV emission line.

Dalla Bontá et al. (2020) study BH masses in AGNs based on single-epoch spectra. They used the compilation of RM AGNs by Bentz & Katz (2015) and the AGNs from the SDSS-RM project as well. These authors find that the line dispersion of the C IV emission line is a better proxy for estimating the BH mass than the full width at half maximum (FWHM). They find that in addition to luminosity and line width, a third parameter is required to obtain accurate masses, and this parameter seems to be the Eddington ratio, and they present empirical relations for estimating BH masses from the $H\beta$ and C IV emission lines.

Nevertheless, because for high-luminosity, high-redshift ($z \sim 3$), quasars there are no low-ionization line RM measurements and because most measurements that can be obtained are of the C IV line, it is interesting to estimate the BH mass and to check its correlation with luminosity, even given the above limitations. We note that from our mean spectra (Figure 1), we find that the C IV emission line is not broader and not blueshifted relative to the $\text{Ly}\alpha$ emission line. Thus, the mass estimates of the objects in our sample may be more reliable because our objects are free from some of the above limitations that discourage the use of C IV for mass estimates.

For simplicity and given the very basic assumptions, we use the equation given by Kaspi et al. (2000; Equation (5) therein), where the FWHM of the line is used as the BLR cloud velocity, and it is corrected by a factor of $\sqrt{3}/2$ to account for velocities in three dimensions. The FWHMs we use are listed in Table 6 together with the derived masses. Figure 10 shows the BH mass and UV luminosity relations for the 38 AGNs listed in Table 6. A fit using the FITEXY method (solid line in Figure 10) is

$$\frac{M_{\text{BH}}}{10^7 M_{\odot}} = (1.70_{-0.58}^{+0.99}) \left(\frac{\lambda L_{\lambda}(1350 \text{ \AA})}{10^{43} \text{ erg s}^{-1}} \right)^{0.45 \pm 0.06}, \quad (3)$$

and for the BCES method (dashed line in Figure 10), it is

$$\frac{M_{\text{BH}}}{10^7 M_{\odot}} = (0.87_{-0.25}^{+0.35}) \left(\frac{\lambda L_{\lambda}(1350 \text{ \AA})}{10^{43} \text{ erg s}^{-1}} \right)^{0.56 \pm 0.05}. \quad (4)$$

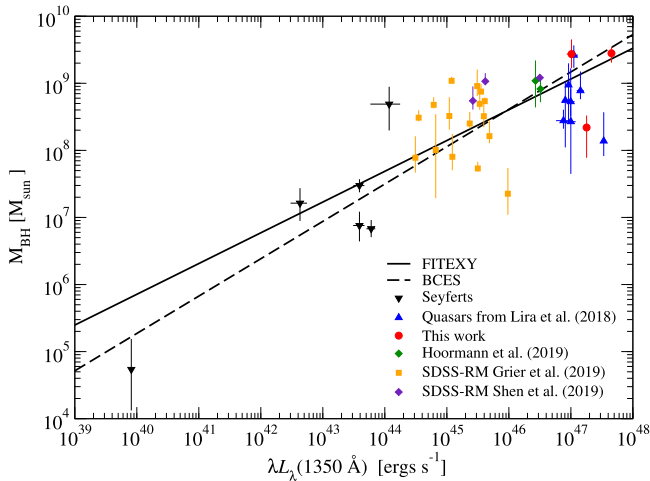


Figure 10. BH mass estimate–UV luminosity relation.

Table 7
Black Hole Mass Estimates from H β Reverberation Mapping

Object	$\log M_{\text{BH}}$
NGC 3783	$7.42^{+0.13}_{-0.14}$
NGC 7469	$6.99^{+0.09}_{-0.01}$
3C 390.3	$8.48^{+0.06}_{-0.08}$
NGC 4151	$7.60^{+0.07}_{-0.06}$
NGC 5548	$7.72^{+0.02}_{-0.02}$

Note. Measurements from the database of Bentz & Katz (2015) in units of $\log M_{\odot}$. Note that the front page of the database lists the averaged mass measurements from all lines, and here we list the mass measurements from the H β line alone.

For these data the Pearson correlation coefficient is 0.79 with a significance level of 5.4×10^{-9} , and the Spearman rank-order correlation is 0.56 with a significance level of 2.5×10^{-4} . The intrinsic scatter using the Tremaine et al. (2002) procedure is 240%.

Theoretically, we expect $M_{\text{BH}} \propto L^{0.5}$, which emerges because $M_{\text{BH}} \propto V^2 r$ and because it is found that $r \propto L^{0.5}$, thus also the BH mass will be proportional to $L^{0.5}$. Because the velocity of the BLR (taken here as the FWHM of the line) does not evolve with the luminosity, it only introduces scatter in the BH mass for a given luminosity; thus the scatter in this relation is larger than the scatter found earlier between the size of the BLR and the luminosity. It should also be noted that the sample in Table 6 does not represent the AGN population in luminosity or in BH mass; thus, the relations found in Equations (3) and (4) may relate more to the way in which the sample was selected, i.e., all objects with significant C IV BLR size measurements.

For five of the six Seyfert AGNs in Table 6 there are BH mass estimates from H β RM. In Table 7 we list these BH mass estimates as given in the database of Bentz & Katz (2015).¹⁴ From a comparison of these mass estimates to our estimates from the C IV line in Table 6, we find that for NGC 7469 and 3C 390.3, the BH mass estimates from the two lines are within the 1σ uncertainties (i.e., the 1σ uncertainties overlap). For NGC 3783 and NGC 4151, the BH mass estimates are within

the 1.5σ uncertainties (if we add the σ from both measurements), and for NGC 5548, they are within 2σ . This resemblance in the mass estimates for the two emission lines increases the confidence in these results and in the ability of the RM method to give consistent mass estimates.

5. Summary

We have reported the final results from a 13 yr spectrophotometric RM campaign on high-luminosity quasars. The spectrophotometric observations were supplemented by 18 yr of photometric monitoring, which improved the cadence and the accuracy of the spectrophotometric continuum light curves by adding to them the photometric light curves.

All 11 objects with photometric light curves display continuum variability of 10%–70% over about six years in the rest frame. This value is similar to that reported in Paper I with data over a period that was about one-third of the current one. Six of the 11 objects were monitored spectroscopically. We identified C IV emission-line time lags for 3 objects, indicating C IV emission-line region sizes of about 100 to 250 light days. Together with data from previous studies, we have constructed a C IV BLR size–UV luminosity relation over eight orders of magnitude in UV luminosity; the slope of 0.45 ± 0.04 is consistent with previous studies and with photoionization theory.

Although all our monitored AGNs show significant continuum variation, only in about half of them did we measure C IV time lag (the same fraction was also found by Lira et al. 2018). This may indicate that the ionizing continuum behaves differently from the 1350 Å continuum we measured in this study.

Although C IV is not a preferred line for the central BH mass determination, we derive the mass for the 19 objects with proper C IV RM data. We find that the mass scales approximately as the square root of the UV luminosity, but with a large scatter. The scatter probably results at least partly from the drawbacks of the C IV line for BH mass measurement, but probably also includes an intrinsic scatter in that relation for AGNs, e.g., different velocities for given BLR size.

Our results demonstrate that for RM of high-luminosity quasars to succeed, a long monitoring period of about a decade or more is needed, and a large enough sample is required in order to be able to detect the responses to continuum variations in at least some of the objects in the sample. Current studies for C IV RM mostly cover the UV luminosity range above $10^{43} \text{ erg s}^{-1}$, and more studies are needed to cover the lower-luminosity range of the AGNs phenomenon.

We are grateful to the staffs of WO and HET for their great assistance in executing this long-term program. Special thanks go to John Dann, Ezra Mashal, and Sami Ben-Gigi of the WO and to Gary Hill of the HET for devoted technical support of this project through the years. The Hobby-Eberly Telescope (HET) is a joint project of the University of Texas at Austin, the Pennsylvania State University, Stanford University, Ludwig-Maximilians-Universität München, and Georg-August-Universität Göttingen. The HET is named in honor of its principal benefactors, William P. Hobby and Robert E. Eberly. The Marcario Low-Resolution Spectrograph is named for Mike Marcario of High Lonesome Optics, who fabricated several optics for the instrument, but died before its completion; it is a joint project of the Hobby-Eberly Telescope partnership and the Instituto de Astronomía de la Universidad Nacional Autónoma de México. We gratefully acknowledge the financial support of

¹⁴ <http://www.astro.gsu.edu/AGNmass/>

the Colton Foundation at Tel-Aviv University (S. K.), NASA ADP grant 80NSSC18K0878 and the V.M. Willaman Endowment (W. N. B). This research has made use of the NASA/IPAC Extragalactic Database (NED) which is operated by the Jet Propulsion Laboratory, California Institute of Technology, under contract with the National Aeronautics and Space Administration.

Appendix Photometric Light Curves and Analysis

Figures 11 and 12 and Table 8 present the R - and B -band light curves of the five quasars that were observed only photometrically at the Wise Observatory. Figure 13 and Table 9 also present the B -band light curves for the six spectroscopically monitored quasars for which the R -band light curves were merged into the spectroscopic continuum light curves and are shown in Figures 2–7

In several cases, multiple observations of a given quasar were obtained during the same night; these measurements were averaged into one point in the light curve. Apparent magnitude calibration was achieved by using nonvariable stars in the field of each quasar, with B and R magnitudes taken from the

USNO-A2.0 catalog.¹⁵ The number of observations as well as statistical information about the light curves are provided at the bottom of Table 3.

We have cross correlated the photometric B - and R -band light curves for all objects. The CCF results are listed in Table 10, and two examples of the CCFs are shown in Figure 14. The significance of the results is not high because the monthly sampling rate limits the detected time lags. Moreover, there is probably a mixture of lines and continuum in some of these broad bands. This mixture will cause the detected variations in the broad bands to be superpositions of the continuum variations and the line variations, which are not in phase. This limits our ability to determine the time lags between the red and blue continuum in these AGNs. Nevertheless, three objects (SBS 1116+603, SBS 1425+606, and S5 2017+744) formally show negative time lags both in their centroid and in the peak of the CCF. This formally means that the R -band light curve is lagging the B -band light curve. Although we do not refer to these results as highly significant, this is in accordance with results from other RM studies that found that the red continuum emission of AGNs is lagging the blue continuum emission (e.g., Collier et al. 1998; Chelouche et al. 2019; Edelson et al. 2019).

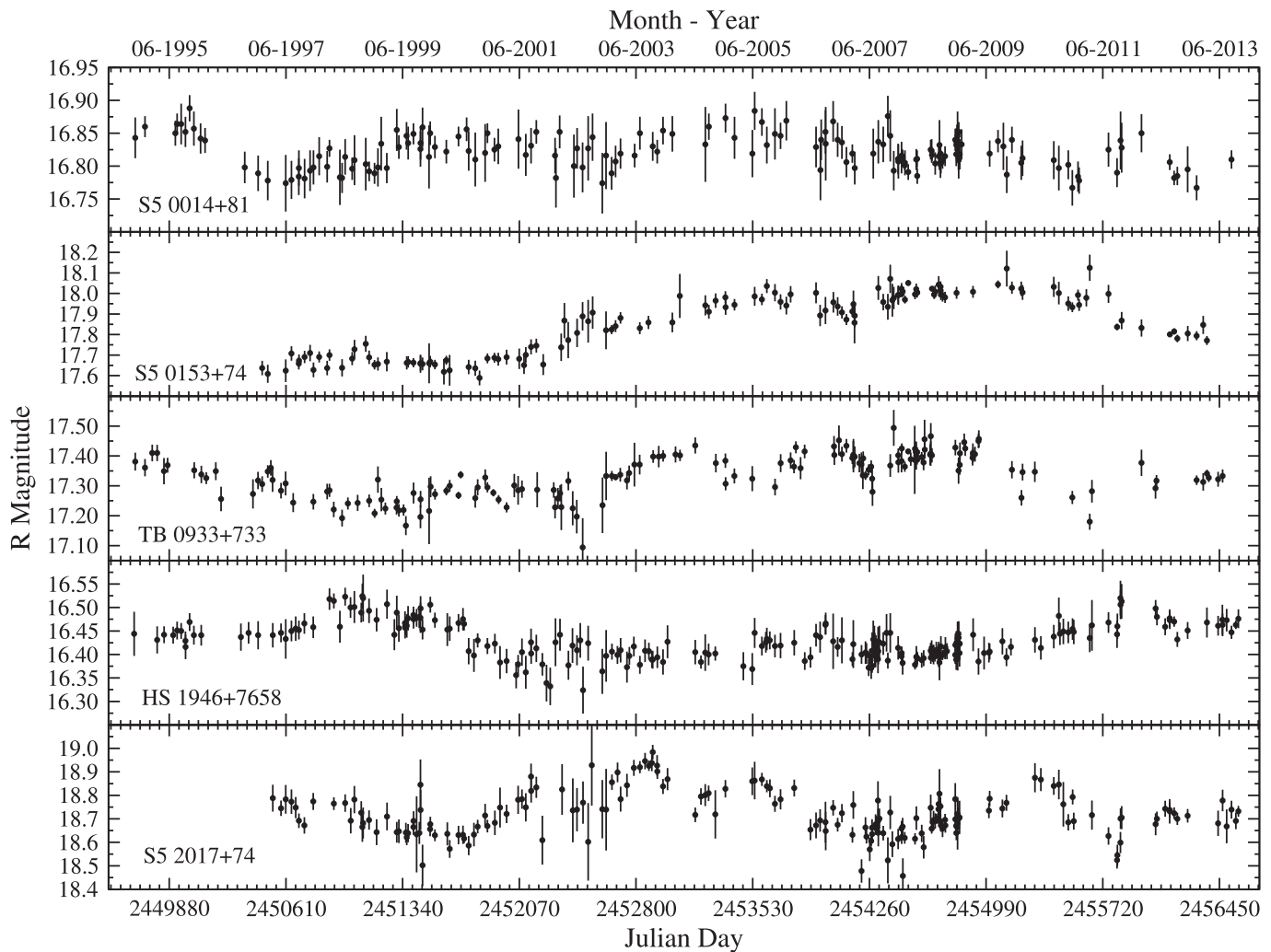


Figure 11. R -band light curves of the five quasars that have no spectroscopic observations.

¹⁵ see: http://brucegary.net/dummies/USNO-A2_Method.htm

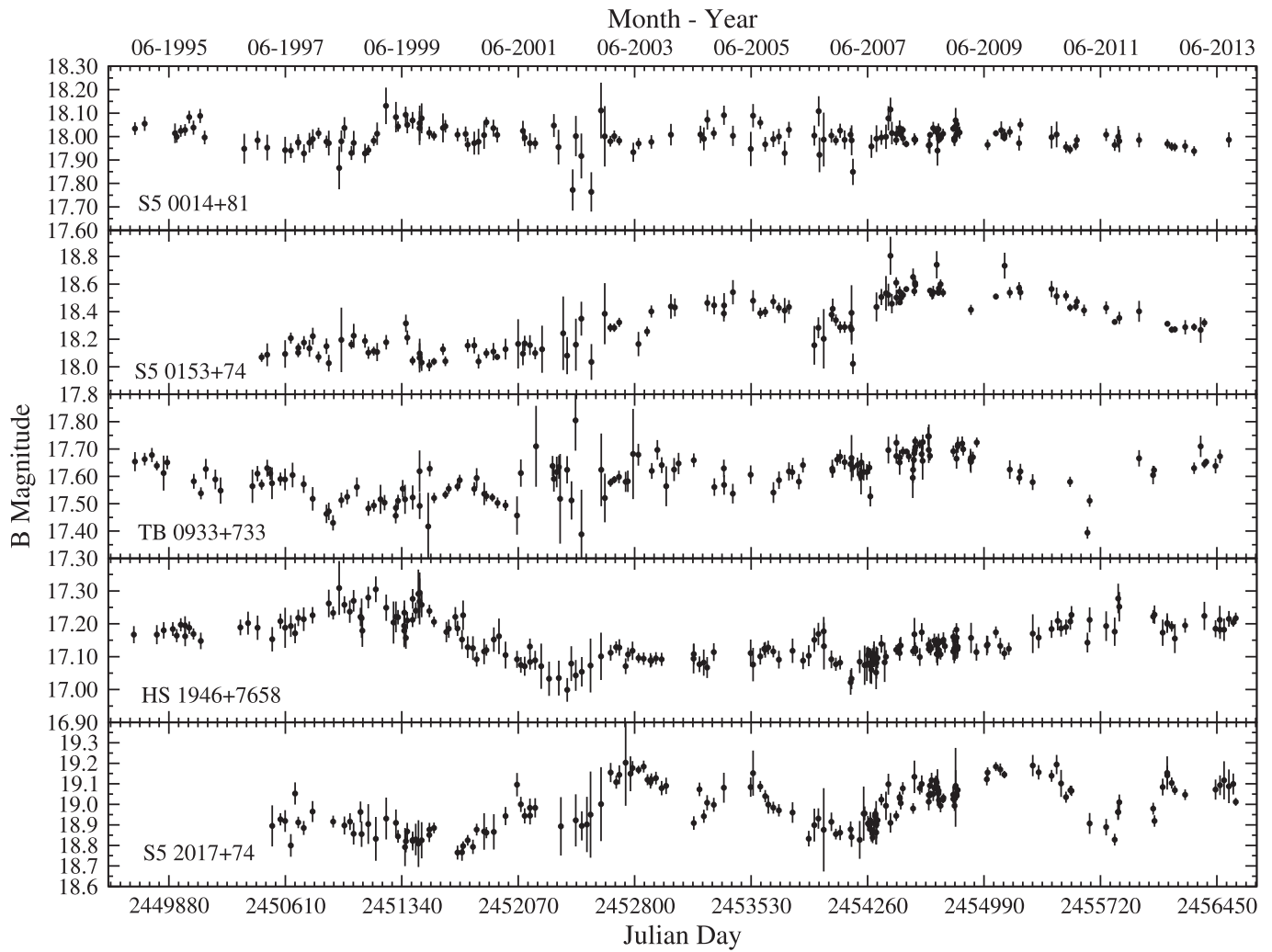


Figure 12. *B*-band light curves of the five quasars that have no spectroscopic observations.

Table 8
R- and *B*-band Light Curves for Five Objects

JD	Apparent Magnitude
S5 0014+81 <i>R</i> band	
2449667.28	16.843 ± 0.031
2449728.24	16.860 ± 0.016
2449918.57	16.850 ± 0.019
2449929.52	16.864 ± 0.016
2449954.46	16.864 ± 0.031
2449981.42	16.852 ± 0.023
2450007.39	16.888 ± 0.020
2450034.32	16.857 ± 0.026
2450076.22	16.842 ± 0.023
2450104.20	16.839 ± 0.019

Note. Table 8 is presented in its entirety in the electronic edition of the Astrophysical Journal. A portion is shown here for guidance regarding its form and content.

(This table is available in its entirety in machine-readable form.)

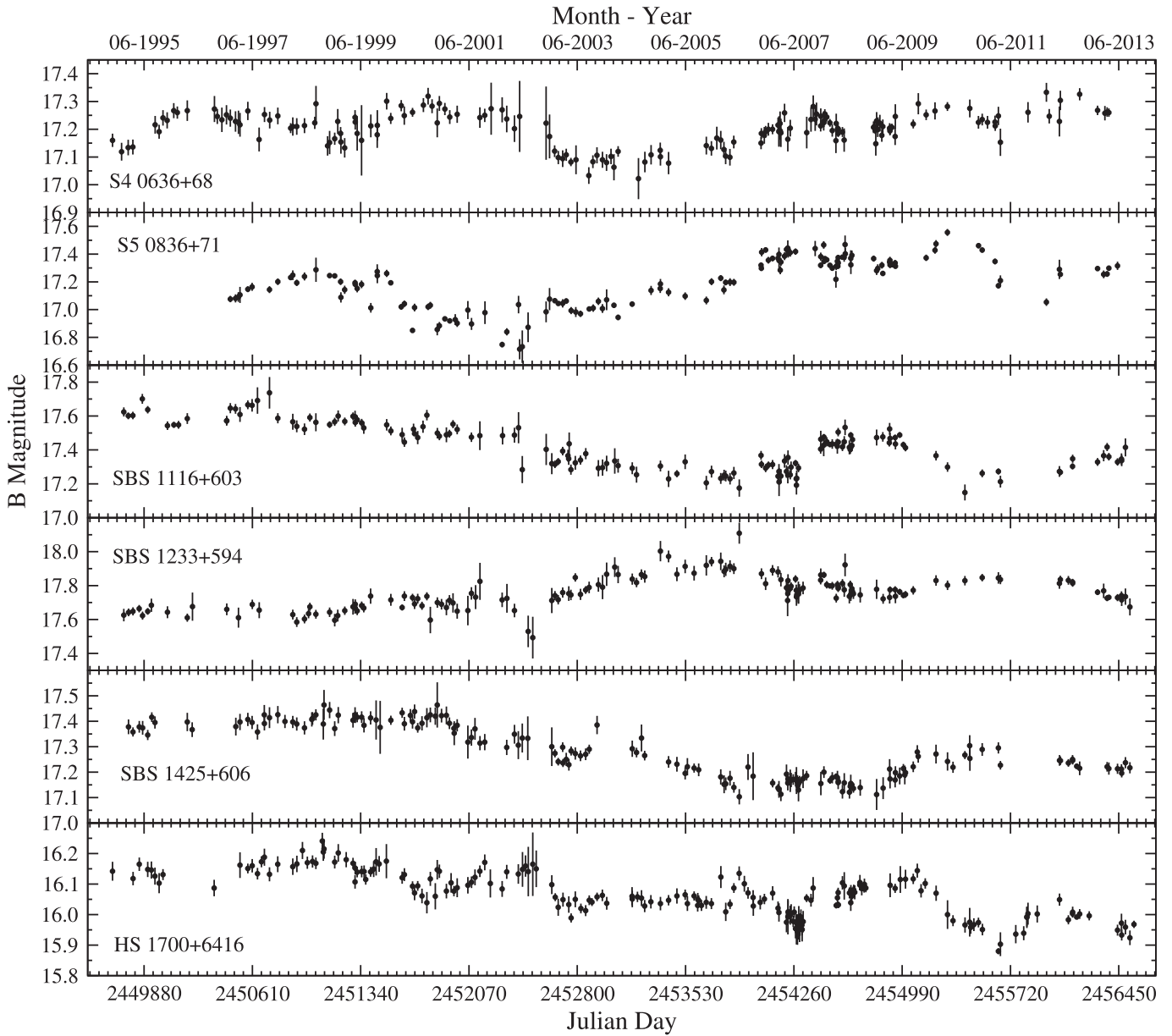


Figure 13. *B*-band light curves of the six quasars with spectroscopic observations. The *R*-band light curves of these objects were combined with the spectroscopic data as explained in Section 3.1, and they are shown in Figures 2 to 7.

Table 9
B-band Light Curves for Six Objects

JD	Apparent Magnitude
S5 0636+68 <i>B</i> band	
2449667.43	17.160 ± 0.024
2449728.43	17.119 ± 0.032
2449773.25	17.134 ± 0.028
2449804.22	17.136 ± 0.027
2449954.57	17.216 ± 0.032
2449981.59	17.191 ± 0.025
2450007.51	17.241 ± 0.028
2450035.48	17.232 ± 0.029
2450080.23	17.267 ± 0.027

Note. Table 9 is presented in its entirety in the electronic edition of the *Astrophysical Journal*. A portion is shown here for guidance regarding its form and content.

(This table is available in its entirety in machine-readable form.)

Table 10
Time Lags of ICCF between *B* and *R* Bands

Object	τ_{Centroid}	τ_{Peak}
S5 0014+81	-4^{+59}_{-76}	6^{+59}_{-106}
S5 0153+74	46^{+199}_{-71}	-18^{+118}_{-32}
S4 0636+68	6^{+49}_{-51}	4^{+66}_{-39}
S5 0836+71	63^{+27}_{-43}	6^{+29}_{-11}
TB 0933+733	2^{+43}_{-67}	2^{+48}_{-62}
SBS 1116+603	-145^{+85}_{-65}	-114^{+89}_{-26}
SBS 1233+594	-43^{+63}_{-72}	-16^{+36}_{-74}
SBS 1425+606	-264^{+39}_{-146}	-154^{+134}_{-181}
HS 1700+6416	-75^{+55}_{-20}	6^{+4}_{-81}
HS 1946+7658	-33^{+78}_{-72}	8^{+37}_{-118}
S5 2017+744	-87^{+62}_{-58}	-108^{+103}_{-52}

Note. Time lags are given in days in the observed frame. A minus sign before the time lag means that formally, the *R* band is lagging behind the *B* band.

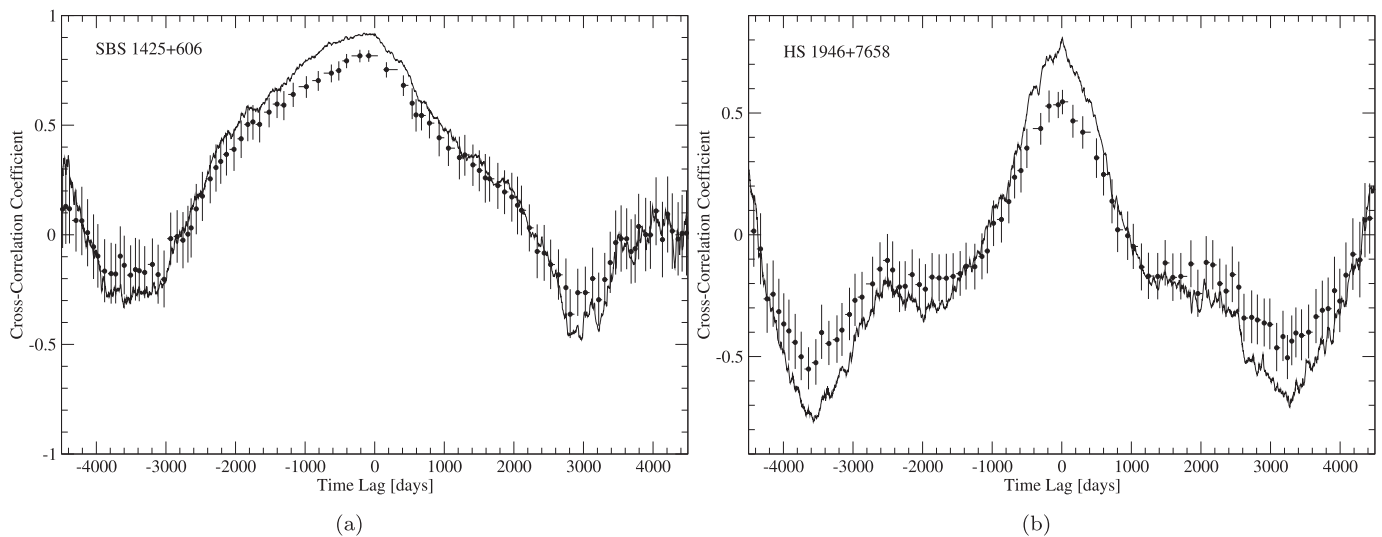


Figure 14. Cross correlation between the B and R bands in (a) SBS 1425+606 and (b) HS 1946+7658. The ICCF is plotted as the solid line, and the ZDCF is plotted as black points with uncertainties.

ORCID iDs

Shai Kaspi <https://orcid.org/0000-0002-9925-534X>
 W. N. Brandt <https://orcid.org/0000-0002-0167-2453>
 Dan Maoz <https://orcid.org/0000-0002-6579-0483>
 Hagai Netzer <https://orcid.org/0000-0002-6766-0260>
 Donald P. Schneider <https://orcid.org/0000-0001-7240-7449>
 Ohad Shemmer <https://orcid.org/0000-0003-4327-1460>
 C. J. Grier <https://orcid.org/0000-0001-9920-6057>

References

- Akritas, M. G., & Bershad, M. A. 1996, *ApJ*, **470**, 706
 Alexander, T. 1997, in *Astronomical Time Series*, ed. D. Maoz, A. Sternberg, & E. M. Leibowitz (Dordrecht: Kluwer), 163
 Baldwin, J. A. 1977, *ApJ*, **214**, 679
 Baskin, A., & Laor, A. 2005, *MNRAS*, **356**, 1029
 Bentz, M. C., & Katz, S. 2015, *PASP*, **127**, 67
 Chelouche, D., Pozo Nuñez, F., & Kaspi, S. 2019, *NatAs*, **3**, 251
 Coatman, L., Hewett, P. C., Banerji, M., et al. 2017, *MNRAS*, **465**, 2120
 Collier, S. J., Horne, K., Kaspi, S., et al. 1998, *ApJ*, **500**, 162
 Constantin, A., Shields, J. C., Hamann, F., et al. 2002, *ApJ*, **565**, 50
 Dalla Bontá, E., Peterson, B. M., Bentz, M. C., et al. 2020, *ApJ*, **903**, 112
 De Rosa, G., Peterson, B. M., Ely, J., et al. 2015, *ApJ*, **806**, 128
 Dietrich, M., Hamann, F., Shields, J. C., et al. 2002, *ApJ*, **581**, 912
 Du, P., Brotherton, M. S., Wang, K., et al. 2018, *ApJ*, **869**, 142
 Du, P., Hu, C., Lu, K.-X., et al. 2015, *ApJ*, **806**, 22
 Du, P., Lu, K.-X., Zhang, Z.-X., et al. 2016, *ApJ*, **825**, 126
 Edelson, R., Gelbord, J., Cackett, E., et al. 2019, *ApJ*, **870**, 123
 Edelson, R., Turner, T. J., Pounds, K., et al. 2002, *ApJ*, **568**, 610
 Edelson, R. A., & Krolik, J. H. 1988, *ApJ*, **333**, 646
 Gaskell, C. M., & Peterson, B. M. 1987, *ApJS*, **65**, 1
 Gaskell, C. M., & Sparke, L. S. 1986, *ApJ*, **305**, 175
 Goad, M. R., Knigge, C., Korista, K. T., et al. 2019, *MNRAS*, **486**, 5362
 Grier, C. J., Shen, Y., Horne, K., et al. 2019, *ApJ*, **887**, 38
 Grier, C. J., Trump, J. R., Shen, Y., et al. 2017, *ApJ*, **851**, 21, [Erratum: 2018, *ApJ*, 868, 76]
 Hill, G. J., Nicklas, H. E., MacQueen, P. J., et al. 1998, *Proc. SPIE*, **3355**, 375
 Hoormann, J. K., Martini, P., Davis, T. M., et al. 2019, *MNRAS*, **487**, 3650
 Jorstad, S., Marscher, A., Larionov, V., et al. 2013, *EPJ Conf.*, **61**, 04003
 Kaspi, S., Brandt, W. N., Maoz, D., et al. 2007, *ApJ*, **659**, 997, (Paper I)
 Kaspi, S., Maoz, D., Netzer, H., et al. 2005, *ApJ*, **629**, 61
 Kaspi, S., Smith, P. S., Netzer, H., et al. 2000, *ApJ*, **533**, 631
 León-Tavares, J., Chavushyan, V., Patiño-Álvarez, V., et al. 2013, *ApJL*, **763**, L36
 Li, I.-H., Shen, Y., Brandt, W. N., et al. 2019, *ApJ*, **884**, 119
 Lira, P., Kaspi, S., Netzer, H., et al. 2018, *ApJ*, **865**, 56, [Erratum: 2020, *ApJ*, 892, 156]
 Mejía-Restrepo, J. E., Trakhtenbrot, B., Lira, P., et al. 2016, *MNRAS*, **460**, 187
 Mejía-Restrepo, J. E., Trakhtenbrot, B., Lira, P., et al. 2018, *MNRAS*, **478**, 1929
 Metzroth, K. G., Onken, C. A., & Peterson, B. M. 2006, *ApJ*, **647**, 901
 Netzer, H. 2020, *MNRAS*, **494**, 1611
 Netzer, H., Lira, P., Trakhtenbrot, B., Shemmer, O., & Cury, I. 2007, *ApJ*, **671**, 1256
 Netzer, H., & Peterson, B. M. 1997, in *Astronomical Time Series*, ed. D. Maoz, A. Sternberg, & E. Leibowitz (Dordrecht: Kluwer Academic Publishers), 85
 Paltani, S., & Türler, M. 2003, *ApJ*, **583**, 659
 Park, D., Woo, J.-H., Denney, K. D., et al. 2013, *ApJ*, **770**, 87
 Peterson, B. M. 1993, *PASP*, **105**, 247
 Peterson, B. M., Bentz, M. C., Desroches, L.-B., et al. 2005, *ApJ*, **632**, 799, [Erratum: 2006, *ApJ*, 641, 638]
 Peterson, B. M., Ferrarese, L., Gilbert, K. M., et al. 2004, *ApJ*, **613**, 682
 Peterson, B. M., Wanders, I., Horne, K., et al. 1998, *PASP*, **110**, 660
 Press, W. H., Teukolsky, S. A., Vetterling, W. T., & Flannery, B. P. 1992, *Numerical Recipes in FORTRAN* (2nd edn.; Cambridge: Cambridge Univ. press)
 Ramsey, L. W., Adams, M. T., Barnes, T. G., et al. 1998, *Proc. SPIE*, **3352**, 34
 Richards, G. T., Kruczek, N. E., Gallagher, S. C., et al. 2011, *AJ*, **141**, 167
 Rodríguez-Pascual, P. M., Alloin, D., Clavel, J., et al. 1997, *ApJS*, **110**, 9
 Saturni, F. G., Trevese, D., Vagnetti, F., Perna, M., & Dadina, M. 2016, *A&A*, **587**, A43
 Schlafly, E. F., & Finkbeiner, D. P. 2011, *ApJ*, **737**, 103
 Shang, Z., Wills, B. J., Wills, D., & Brotherton, M. S. 2007, *AJ*, **134**, 294
 Shaw, M. S., Romani, R. W., Cotter, G., et al. 2012, *ApJ*, **748**, 49
 Shen, Y., Grier, C. J., Horne, K., et al. 2019, *ApJL*, **883**, L14
 Shen, Y., Horne, K., Grier, C. J., et al. 2016, *ApJ*, **818**, 30
 Trakhtenbrot, B., & Netzer, H. 2012, *MNRAS*, **427**, 3081
 Tremaine, S., Gebhardt, K., Bender, R., et al. 2002, *ApJ*, **574**, 740
 Trevese, D., Paris, D., Stirpe, G. M., Vagnetti, F., & Zitelli, V. 2007, *A&A*, **470**, 491
 Trevese, D., Perna, M., Vagnetti, F., Saturni, F. G., & Dadina, M. 2014, *ApJ*, **795**, 164
 Trevese, D., Stirpe, G., Vagnetti, F., Zitelli, V., & Paris, D. 2006, in *ASP Conf. Ser.*, 360 (San Francisco, CA: ASP), 201
 Vestergaard, M., & Peterson, B. M. 2006, *ApJ*, **641**, 689
 Vietri, G., Maimeri, V., Kakkad, D., et al. 2020, *A&A*, **644**, A175
 Welsh, W., Robinson, E. L., Hill, G., et al. 2000, *BAAS*, **32**, 1458
 White, R. J., & Peterson, B. M. 1994, *PASP*, **106**, 879
 Yu, Z., Kochanek, C. S., Peterson, B. M., et al. 2020, *MNRAS*, **491**, 6045
 Zu, Y., Kochanek, C. S., Kozłowski, S., & Udalski, A. 2013, *ApJ*, **765**, 106
 Zu, Y., Kochanek, C. S., & Peterson, B. M. 2011, *ApJ*, **735**, 80